Post-print version of the paper by Lu et al.
in Int J Cold Region of Science and Technology, 156 (2018) 117-133,
https://doi.org/10.1016/j.coldregions.2018.07.010

Parallel Channels' Fracturing Mechanism during Ice Management Operations. Part I: Theory

Wenjun Lu[1] **Raed Lubbad** **Aleksey Shestov** **Sveinung Løset**

(To be submitted to <Cold Regions Science & Technology> special issue)

Sustainable Arctic Marine and Coastal Technology (SAMCoT), Centre for Research-based Innovation (CRI)

Norwegian University of Science and Technology (NTNU), Trondheim, Norway

[1] Corresponding author
E-mail address: wenjun.lu@ntnu.no (Wenjun Lu)

Post-print version of the paper by Lu et al.
in Int J Cold Region of Science and Technology, 156 (2018) 117-133,
https://doi.org/10.1016/j.coldregions.2018.07.010

Contents

Post-print version of the paper by Lu et al.
in Int J Cold Region of Science and Technology, 156 (2018) 117-133,
https://doi.org/10.1016/j.coldregions.2018.07.010

Abstract

It is frequently observed that long cracks in sea-ice tend to form between parallel channels during ice management operations. The long cracks that develop play an important role in reducing the size of the managed ice floes, which is one of the main goals in an ice management operation. However, the fracture mechanism behind these long cracks remains unclear. To address this issue, a comprehensive study is reported here in two associated papers. In the current paper (i.e., Paper I), an edge-crack theoretical model is proposed to elucidate the parallel channels' fracture mechanism. The proposed theoretical model is partially based on theories regarding ship – level ice interactions and partially based on previous studies on the general ice fracturing mechanism. The edge-crack theoretical model is extensively examined using a separately developed numerical scheme based on the eXtended Finite Element Method (XFEM), which allows for the existence of a singularity field and displacement jump within conventional Finite Elements (i.e.., FEM). The numerical scheme is benchmarked against known asymptotic analytical solutions and field experiments. Afterwards, with the developed numerical scheme, through fitting numerical simulation results in terms of the edge crack's Stress Intensity Factors (SIFs) and a relevant asymptotical analysis, we managed to derive a group of closed-form formulae with wide application ranges. For the current engineering problem, this set of formulae quantifies the maximum parallel channel spacing $h_{\max}$, beyond which the observed parallel channels' fracturing events cease to occur. Moreover, the same numerical scheme is utilised to study parallel channels' fracturing paths. Based on the XFEM-based crack path simulations, a second group of formulae and a numerical recipe were obtained to characterise a simplified crack path. This set of equations enables us to quantify the maximum floe size L_{MCD} that can be generated between two parallel channels and its corresponding floe size ratio. In the sequel paper (i.e., Paper II), these equations are validated by a series of well-controlled field experiments undertaken during the Oden Arctic Technology Research Cruise of 2015 (OATRC2015).

Keywords:

Edge crack; XFEM; Parallel channel; Ice fracture; Ice management; 25

Post-print version of the paper by Lu et al.
in Int J Cold Region of Science and Technology, 156 (2018) 117-133,
https://doi.org/10.1016/j.coldregions.2018.07.010

1 Introduction

An important objective for a physical ice management operation is to reduce the size of drifting ice floes that will interact with downstream protected structures (e.g., platforms and drilling vessels). This can be achieved via different ice management strategies. Typically, several icebreakers are hierarchically deployed upstream and operated with different prescribed patterns to systematically breakdown the incoming large ice floes. The designed operational patterns include circular, elliptical, (linear/arched) racetrack, orbital, and linear patterns (Hamilton et al., 2011a, Hamilton et al., 2016). For all these different patterns, the icebreakers' tracks over ice usually form a series of parallel channels (see Fig. 1a) filled with newly broken ice rubble (i.e., brash ice). Notably, it was often observed that long cracks were formed between parallel channels, leading to a further reduction in ice floe sizes (Farid et al., 2014, Hamilton et al., 2011a). The term 'long cracks', as adopted herein, is to make a differentiation from conventional fracture patterns such as radial and circumferential cracks formed during interactions of level ice and sloping structure (e.g., the bow region of an icebreaker or an offshore structure with a sloping surface at the waterline/ice line). Fig. 1a illustrates one such long crack captured during the Oden Arctic Technology Research Cruise in 2015 (OATRC2015). An overview of OATRC2015 is given by Lubbad et al. (2016); Fig. 1b conceptually highlights the described fracturing phenomena during ice management operations.

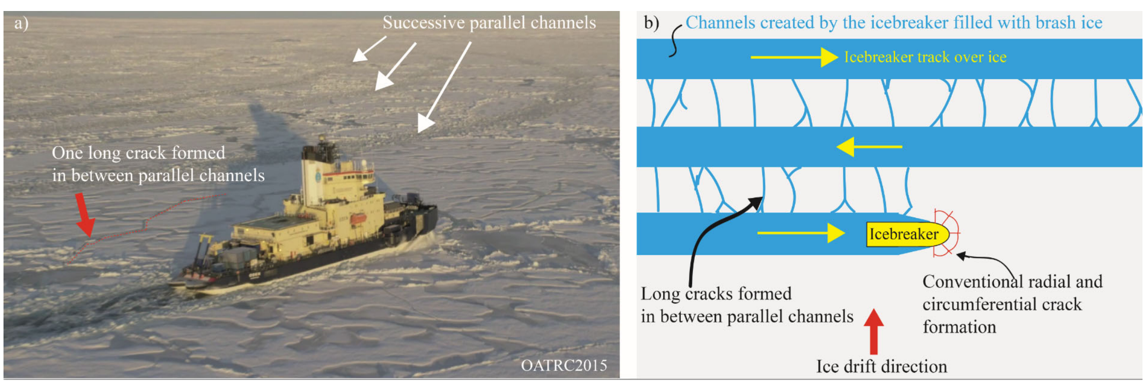

Fig. 1. Illustration of long cracks formed between parallel channels during ice management operations, a) field experiment with icebreaker Oden; b) conceptual abstraction.

Such ice fracturing phenomena are rather important while designing ice management operations. Hamilton et al. (2011a, 2011b) developed a numerical simulator based on ship and ice field kinematics to quantify the performances of different ice management strategies. One critical assumption of the simulation is that ice floes with aspect ratios of 1:1 are 'naturally' generated between two parallel channels. Given the distance between two parallel channels, the downstream managed ice floe size is thus quantified. This assumption was mainly based on field observations, as there exist no theoretical explanations or experimental quantifications. This paper (i.e., Part

I of two sequential papers) seeks to offer a theoretical explanation regarding such an observed 'parallel channels' fracturing mechanism'. The sequel paper (i.e., Part II) reports comparisons between the theoretical results and full-scale data collected by conducting well-controlled experiments in the field. The two papers address and answer practical questions regarding, for example, 'optimised parallel channel spacing' and 'out-going floe size' for specific ice management operations. Moreover, the theoretical formulations presented herein are useful to enhance the capacities of the numerical Simulator for Arctic Marine Structures (SAMS, 2018) so that it can be used to evaluate different ice management strategies. For a description of SAMS, its theoretical background and potential applications, the reader is referred to (Lu, 2014, Lubbad and Løset, 2011, Lubbad and Løset, 2015, Lubbad et al., 2018).

This paper starts with qualitative field observations regarding the ice fracturing phenomena between parallel icebreaker channels. Based on field observations and knowledge regarding ship – level ice interactions, a theoretical model is proposed to address one of the important contributors to the observed long cracks. The theoretical model entails an edge crack's propagation and kinking in the presence of a neighbouring free boundary. Extensive parametric studies were carried out on the theoretical model. All the analyses are carried out with an eXtended Finite Element Method (XFEM) based numerical scheme. The numerical results were further fitted to analytical closed-form formulae conforming to both existing analytical results in limiting scenarios (i.e., asymptotic solutions) and field experiments. In the sequel paper (Paper II), the developed analytical formulations will be verified against a series of well controlled parallel channel tests undertaken during OATRC2015.

2 Observations and Theoretical Model

2.1 Ice Fracturing during Ship – Level Ice Interactions

Before we present the ship – ice interactions under the presence of an adjacent parallel channel, it is beneficial to take a retrospective look into the theory of ship – level ice interactions. This is because the theory can be further extended to the observed 'parallel channels' fracturing mechanism'. Particularly, it is the ice breaking/fracture patterns that are of interest here. It is generally accepted that during ship – level ice interactions, aside from local crushing and potential shearing failure taking place at the contact zone (Enkvist et al., 1979), level ice mainly fails in the bending failure mode. This continuous bending process leads to an identifiable fracture pattern with the consecutive formations of cusps (or half-moon) and wedges along the ship's bow's waterline. Naegle (1980) reviewed the previous literature and noted the general agreement regarding such level ice fracture patterns. However, Naegle also noted that two schools of thinking exist regarding how ice fails at the ship stem. One school favours a bending failure mechanism at the stem (e.g., (Lewis and Edwards, 1969, Milano, 1972, Kotras et al., 1983)), while the other school (e.g., (Kashteljan et al., 1969, Enkvist et al., 1979, Ettema et al., 1989)) suggests that mainly crushing and shearing take place at a ship's stem. Another opinion was later put forward by Lindqvist (1989), who mentioned that continuous crushing occurs only for wedge-shaped bows, and by Valanto (2001), who stated that 'hardly any bow crushing occurs for stems with sufficient radius'. In later studies regarding ship – level ice interactions, without specially treating the potential dominant stem shearing failure, most researchers focused on the cusp and wedge bending failures around the waterline of a ship's entire bow (e.g., (Riska, 2011, Su et al., 2010, Sawamura et al., 2009, Tan et al., 2013, Lubbad and Løset, 2011)). This paper adopts the same 'bending-failure dominant' interaction mechanism to further describe the physics behind the crack formations. Accordingly, the same ice breaking pattern (i.e., cusp- and wedge-shaped crack formations) around a ship's entire bow is adopted herein. Fig. 2 illustrates both a conceptual plot and a perfect real-life local bending failure pattern in sea ice. In terms of the cusp- and wedge-shaped crack formations, two types of crack, i.e., radial and circumferential cracks, are highlighted.

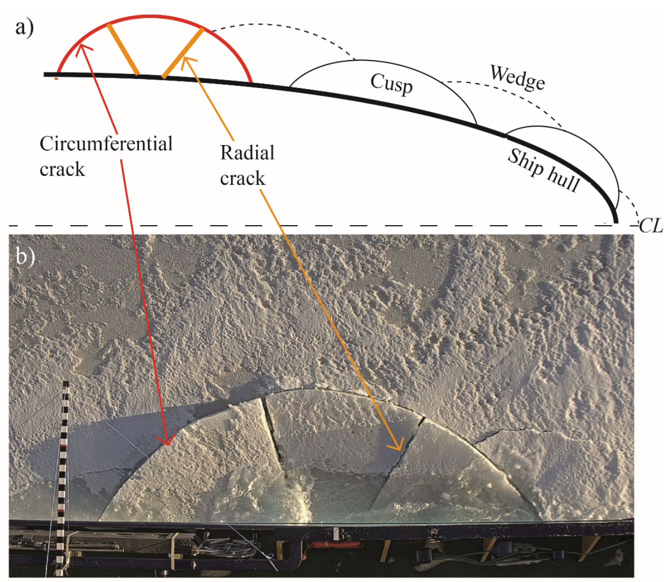

Fig. 2. Cusp- and wedge-shaped crack formations around the ship hull: a) conceptual plot of a series of crack formations; 2) a real-life example showing a perfect crack pattern captured by a camera installed aboard Frej during OATRC2015.

Historically, radial and circumferential cracks have been studied extensively with a theoretical model of 'an infinite/semi-infinite elastic plate on a Winkler type foundation' (see, e.g., a review paper by Kerr (1976)). It is generally agreed that while a large floating ice plate is loaded vertically, radial cracks first emanate from the loading area; afterwards, its final failure is governed by the formation of a circumferential crack. Putting this fracturing mechanism under the context of ship - level ice interaction scenarios, the idealised interaction sequences in Fig. 3 are anticipated. In reality, the formation of contact zones and their associated sequential fractures are not synchronised around the entire ship's bow, as shown in Fig. 3. It can very well be that at any given time point, e.g., t_2, radial cracks are formed at some of the contact zones, whereas circumferential cracks are already formed at some other zones. In addition, the formation of contact zones is rather random both with respect to time and location. Nevertheless, such random contact and fracture processes create an identifiable fracture pattern in the channel (Naegle, 1980, Lewis and Edwards, 1969).

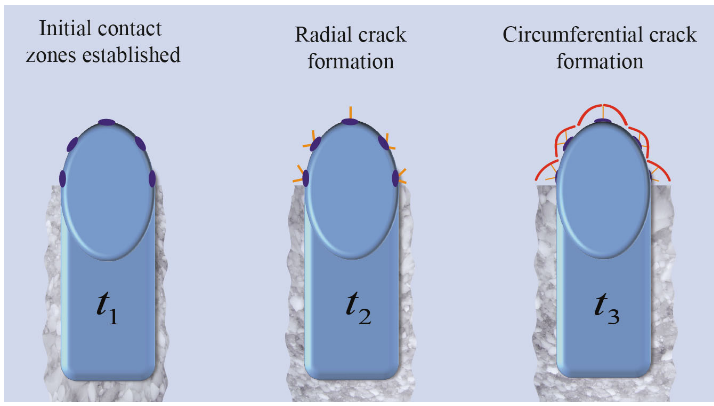

Fig. 3. Sequential formation of radial and circumferential cracks during ship - level ice interactions; $t_3>t_2>t_1$.

2.2 Ice Fracturing with an Adjacent Free Boundary

In terms of ship-ice interactions with the presence of a neighbouring parallel channel, the fracture pattern can be altered. One of the significant consequences is that the nearby free boundary can influence the propagation of radial cracks and promote the formation of long cracks rather than circumferential cracks (i.e., at t_3, the fracture pattern changes from that shown in Fig. 3 to that in Fig. 4). In Fig. 4, the initial radial crack shows a great tendency to be further propagated through the entire ice region reaching the nearby free boundary. Depending on the initial contact's location and the orientation of the initial radial crack, the final long crack shows different paths.

Post-print version of the paper by Lu et al.
in Int J Cold Region of Science and Technology, 156 (2018) 117-133,
https://doi.org/10.1016/j.coldregions.2018.07.010

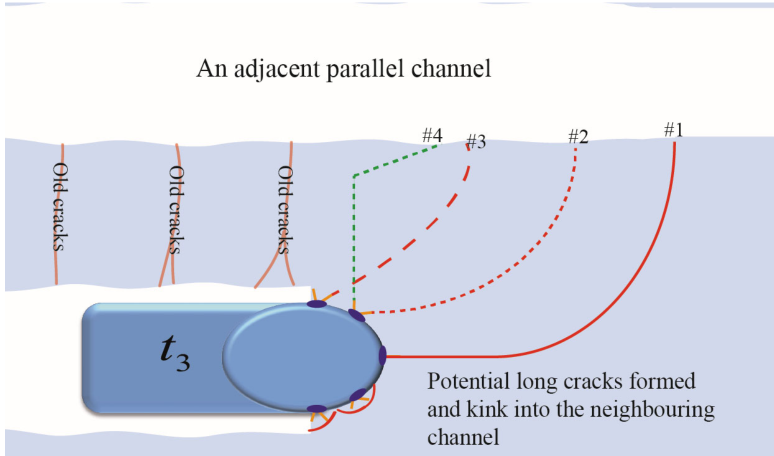

Fig. 4. Potential fracture pattern with the formation of long cracks between two parallel channels.

Fig. 4 demonstrates long Cracks #1 to #4, among which long Cracks #1 to #3 have initial orientations that are almost in line with the ship's surge direction, whereas Crack #4's initial direction is perpendicular to the surge direction. These two types of cracks are termed 'front' and 'side' cracks and were studied previously with a simplified fracture model (Lu et al., 2015d). The sketched long cracks in Fig. 4 are frequently observed in the field. Fig. 5 shows two scenarios of the corresponding cracks observed in the field during the Oden Arctic Technology Research Cruise in 2013 (OATRC2013). The images in Fig. 5 were captured by a 360° camera system installed on board Oden (Bjørklund et al., 2015) and qualitatively illustrate the pattern of long cracks.

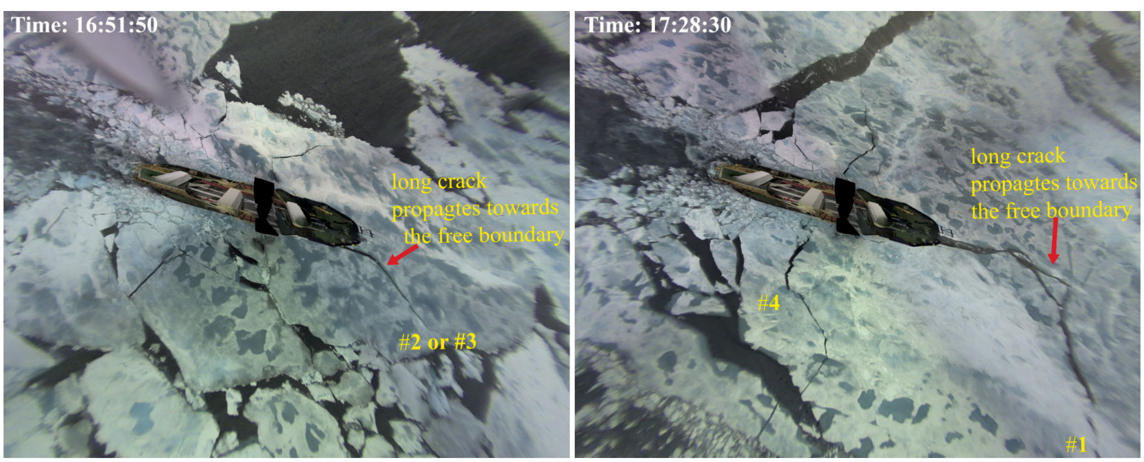

Fig. 5. Formation of long cracks observed in the field in the presence of a neighbouring free boundary on August 28th, 2013, during OATRC2013.

Although the long cracks shown in Fig. 5 were not strictly associated with the parallel channels, the influence of an adjacent free boundary is demonstrated. Among all the potential long cracks (#1-4 shown in Fig. 4 and Fig. 5), we shall primarily focus on Crack #1, which originates from the ship's stem. This is because, among all the potential long crack formations, Crack #1 leads to a greater chance to produce the largest ice floe between two parallel channels. Cracks #1 to #3 are, in many cases, prone to be mutually exclusive (e.g., see Fig. 5). The reason is that once a long crack is formed, other contact zones' pressures are alleviated, leading to lower probabilities to form fractures of similar scale. Supposing that only Crack #1 is occurring, with the absence of Cracks #2 and 3, a relatively large ice floe can be created. During an ice management operation, one primary goal is to effectively fracture ice and reduce the size of ice floes under a certain threshold. By knowing the largest possible ice floes that can be created between two parallel channels via studying the scenario of Crack #1 enables us to quantify this threshold and to establish its relationship with other factors (e.g., ice thickness, channel spacing and contact properties).

2.3 Theoretical Model and Assumptions

Given the fracturing mechanism presented in previous sections, a simplified interaction model and its assumingly equivalent fracture model are proposed in Fig. 6 to address the propagation of Crack #1. In Fig. 6, the channel of interest is located at the port side (left side) of the vessel. The channel spacing (distance from the ship's centreline to the closest edge of the channel) is denoted h. The ice floe is assumed to be infinitely large (i.e., $H \gg h$ and $L \gg h$) to simplify the theoretical analysis (i.e., additional free boundaries are excluded). At the ship's stem, we focus on the case with a radial crack A_0 that is initially developed in the surge direction. Within the interaction zone, a pair of wedging-out forces F_Y and a force component in the surge direction F_X can be identified acting on the ice floe (see Fig. 5). Not plotted in the figure is the out-of-plane vertical force component F_Z, which is primarily responsible for creating radial cracks (e.g., A_0) and potential circumferential cracks. For the current paper, the formation of long cracks is essentially a splitting problem due to in-plane force components F_X and F_Y (Bhat et al., 1991, Bhat, 1988, Dempsey et al., 1993) as plotted in Fig. 6a.

Post-print version of the paper by Lu et al.
in Int J Cold Region of Science and Technology, 156 (2018) 117-133,
https://doi.org/10.1016/j.coldregions.2018.07.010

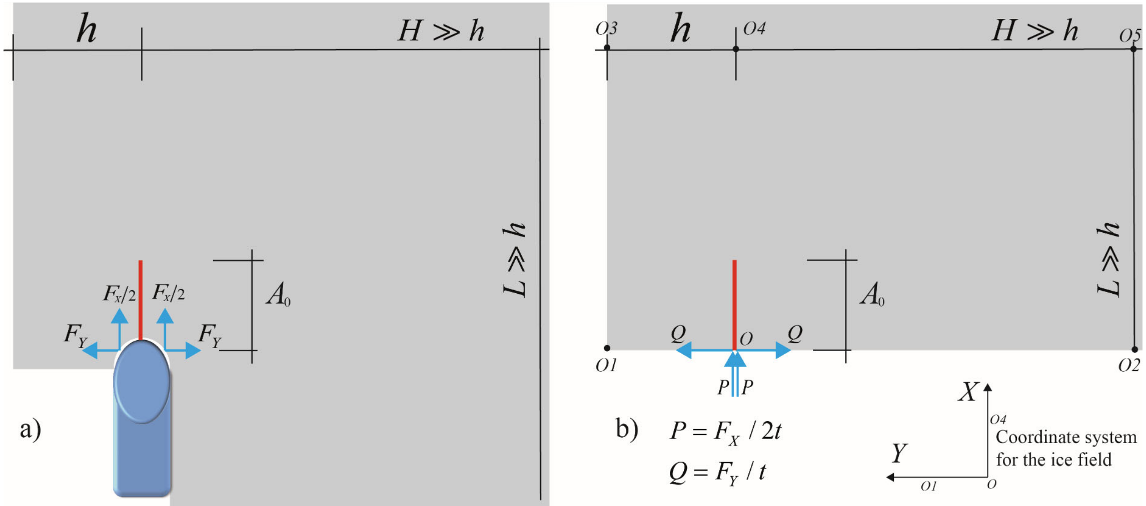

Fig. 6. Proposed theoretical model for the formation of long cracks with the presence of an adjacent parallel channel (note that the sketched sizes are not in scale), a) actual engineering problem; b) a simplified two dimensional model involving an edge crack in a quarter plane.

Notably, the cracked geometry involving an edge crack in Fig. 6b was extensively studied in the early literature under various loading conditions. General solutions to this cracked geometry have wide engineering applications in relation to edge dominated cracking phenomena (Thouless and Evans, 1990, Thouless et al., 1987). In ice research communities, the same edge cracked geometry has been adopted to address ice fractures at different scales. For example, the spalling fracture (flaking) of an ice sheet while interacting with a vertical structure was studied by a similar model (Evans et al., 1984). In the spalling fracture model (see Fig. 7a), an ice-structure contact pressure is applied onto the surface of $O1-O2$. In this context, the surface $O1-O2$ represents the ice thickness direction (i.e., ice thickness = $H + h$). Because of the tri-axial stress state within the ice thickness, an initial crack A_0 at a location O tends to open and kink towards the ice surface (i.e., $O1-O3$), thus creating a spall (i.e., within $O1-O-O4-O3$) off the intact ice sheet. Moreover, Renshaw and Schulson (2001) utilised the same cracked geometry at a much smaller scale (i.e., approximately 1 to 4 mm) to elucidate the mechanisms of comb-like secondary cracks in the scenario of brittle compressive failures. In the comb-crack model (see Fig. 7b), due to a compressive force, a frictional drag along the $O2-O1$ surface creates a clockwise overturning moment upon micro-plates (e.g., $O1-O-O4-O3$), thereby leading to the successive bending failures of micro-plates and creating the observed secondary cracks (Schulson and Duval, 2009).

Post-print version of the paper by Lu et al.
in Int J Cold Region of Science and Technology, 156 (2018) 117-133,
https://doi.org/10.1016/j.coldregions.2018.07.010

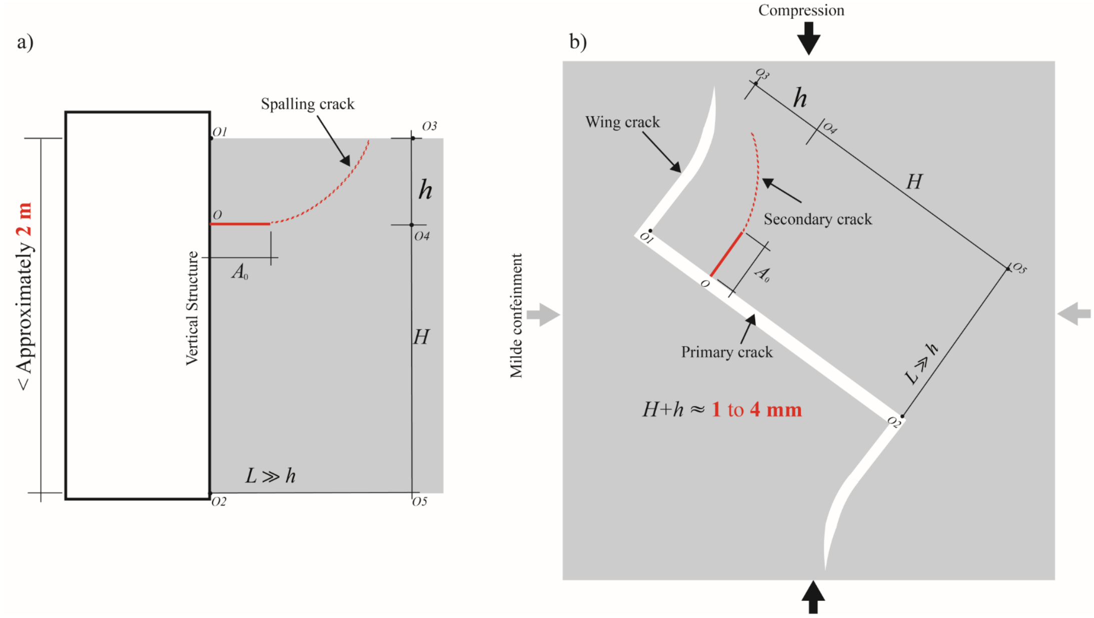

Fig. 7. Previous application of the proposed fracture model in ice research: a) cross section of an ice – structure contact in the thickness direction with a scale within 2 metres; b) the secondary crack development model at ice grain scale.

Both of the aforementioned applications implicitly adopted the Linear Elastic Fracture Mechanics (LEFM) theory, which is yet subjected to discussions given their limited physical scales (i.e., < 2 m for the case in Fig. 7a and approximately 1 to 4 mm for the case in Fig. 7b, respectively). This is because the presence of a Fracture Process Zone (FPZ) ahead of a crack tip in quasi-brittle materials (e.g., ice) would invalidate LEFM given the limited cracked body size (Dempsey, 1991, Dempsey et al., 1999a, Bažant and Planas, 1998). Without detailed reasoning, Bažant (2002a, 2002b) noted that the FPZ's size for sea ice is approximately 40 cm and several metres in the vertical and horizontal directions, respectively. Furthermore, Mulmule and Dempsey (2000), after rigorous model calculations and a series of field measurements (Dempsey et al., 1999a), concluded that LEFM becomes valid only after a cracked body size $\geq 12\ell_{ch}$, which is approximately 0.5 to 3.6 m (see the detailed reasonings in, e.g., (Lu et al., 2015b, Lu et al., 2015d)) given the definition of characteristic length ℓ_{ch} introduced by Hillerborg et al. (1976) and a range of fracture energy values available in the literature (Dempsey et al., 1999a, Mulmule and Dempsey, 1998, Schulson and Duval, 2009). In comparison, the parallel channel fracturing problem in Fig. 6 is at a much larger scale, which is in the range of tens to hundreds of metres. Even if indeed a large FPZ exists for sea ice, the cracked body's size (Fig. 6b) in our application is large enough such that LEFM theory becomes valid. Therefore, one major assumption in this paper is the adoption of LEFM theories to study the long cracks developed in between two parallel channels with the edge crack model. In terms of the force conditions in the proposed cracked body in

Fig. 6b, we follow an existing paper (Freund, 1978) and introduce additional force components in Eq. (1), with t being ice thickness.

$$\begin{aligned} P &= F_X / 2t \\ Q &= F_Y / t \end{aligned} \tag{1}$$

3 Methods

With the proposed edge crack model in Fig. 6b, we are to establish the relationship among geometrical factors (i.e., h and A_0), crack propagation criteria related terms (i.e., SIFs K_I and K_{II}) and the eventual crack propagating path. Ultimately, we shall address practical questions such as 1) what is the maximum channel spacing $h_{\max}$ beyond which the long crack ceases to develop and 2) what is the maximum floe size $L_{\max}$ that can be produced between two parallel channels with a given spacing. In this paper, an XFEM based approach is developed to evaluate crack A_0 's propagation. During the course of crack propagation, we assume that a quasi-static equilibrium always exists, i.e., before each crack segment A_i 's advancement (i.e., $A_i \to A_{i+1}$), the overall SIF $K_{tot}(A_i) = K_{IC}$.

3.1 Calculation of Stress Intensity Factors

To evaluate the SIFs for the edge cracked body in Fig. 6b, we first consider the two asymptotic scenarios in Fig. 8, for which analytical solutions are available in the existing literature.

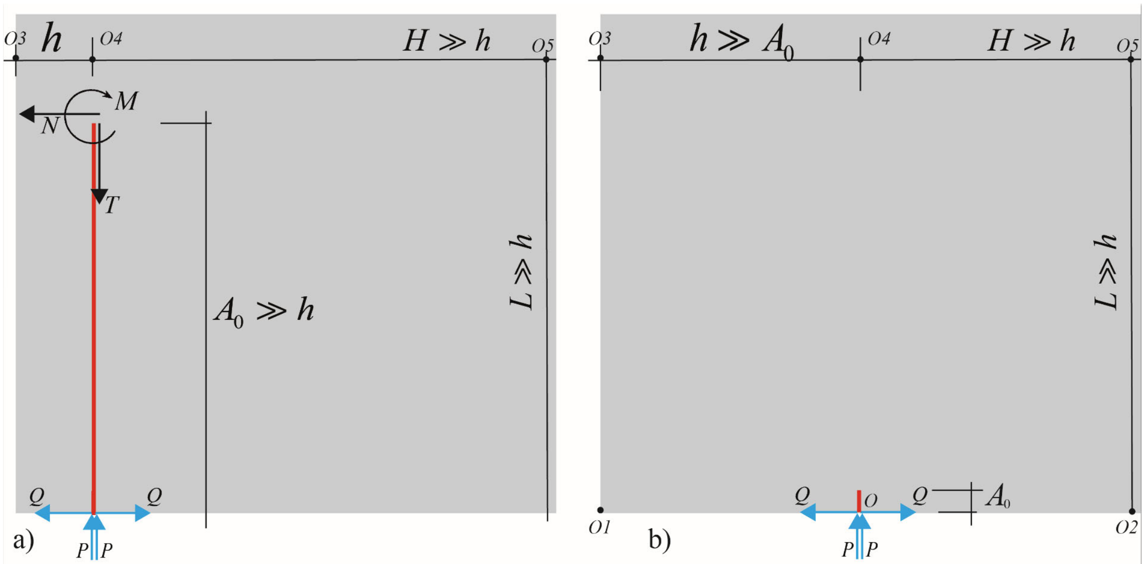

Fig. 8. Two asymptotic scenarios of the edge crack model in Fig. 6b with a) $A_0 \gg h$ and b) $h \gg A_0$.

3.1.1 Asymptotic solution for the case of long crack

For the long crack scenario (i.e., $A_0 \gg h$) in Fig. 8a, the SIFs are written in Eq. (2) according to Dyskin et al. (2000) (the solutions were originally from Zlatin and Khrapkov (1990, 1986)) by considering a semi-infinite beam's solutions under a combined total force (N and T) and moment (M) at the crack tip.

$$\begin{gathered}\begin{bmatrix} K_I^{beam} \\ K_{II}^{beam} \end{bmatrix} = K_M M h^{-3/2} + K_N N h^{-1/2} - (K_T - \frac{1}{2} K_M) T h^{-1/2} \\ K_M = \begin{bmatrix} 1.932 \\ 1.506 \end{bmatrix}, \quad K_N = \begin{bmatrix} 1.951 \\ -0.032 \end{bmatrix}, \quad K_T = \begin{bmatrix} 0.4346 \\ -0.5578 \end{bmatrix}\end{gathered} \tag{2}$$

Considering the external forces, which lead to $M = QA_0$, $N = Q$, and $T = -P$, the long crack's asymptotic solutions are formulated in Eq. (3).

$$\sqrt{h} \begin{bmatrix} K_I^{beam} \\ K_{II}^{beam} \end{bmatrix} = \begin{bmatrix} 1.932(A_0/h) + 1.951 \\ 1.506(A_0/h) - 0.032 \end{bmatrix} Q - \begin{bmatrix} 0.5314 \\ 1.3108 \end{bmatrix} P \tag{3}$$

Eq. (3) shows that the crack parallel force P tends to close the crack and that the crack orthogonal force Q is trying to open the crack. The influences from both of these force components upon SIFs are considered in this paper.

3.1.2 Asymptotic solution for the case of short crack

For the short crack scenario (i.e., $h \gg A_0$) in Fig. 8b, the SIFs can be written as the summation of two parts in Eq. (4) according to a similar study conducted by Dyskin et al. (2000).

$$K_i = K_{i0} + \Delta K_i^{dip} \qquad (i = I, II) \tag{4}$$

According to Dyskin et al. (2000), in the scenario of $h \gg A_0$, the leading term K_{i0} denotes the solution as if the 'nearby' free boundary is infinitely far away (i.e., $h = \infty$). In this regard, the solutions for K_{i0} in Fig. 8b with $h = \infty$ can be found in the literature (e.g., (Freund, 1978, Dempsey and Mu, 2014, Tada et al., 2000)) and are written in Eq. (5).

$$\sqrt{h}\begin{bmatrix} K_{I0} \\ K_{II0} \end{bmatrix} = \sqrt{\frac{4\pi}{\pi^2 - 4}}\left(\frac{A_0}{h}\right)^{-1/2}\begin{bmatrix} Q - \dfrac{2}{\pi}P \\ 0 \end{bmatrix} \tag{5}$$

The other term, ΔK_i^{dip}, takes into account the influence of the free boundary. Based on the dipole asymptotic method, Dyskin et al. (2000) derived the closed form of ΔK_i^{dip} for the case of an embedded crack, demonstrating the term's functional dependency upon $(A_0 / h)^{3/2}$. In this paper, we will assume a similar functional dependency such that $\Delta K_i^{dip} = \varepsilon_3 (A_0 / h)^{\varepsilon_4}$, for which the parameters ε_3 and ε_4 are fitted from numerical simulation results.

3.1.3 Proposed solution for the case of arbitrary crack length

Having obtained the above two asymptotic solutions, we adopt Eq. (6) with parameters ε_1, ε_2, ε_3 and ε_4 (to be fitted by numerical results) to construct the complete solution of SIFs for the edge cracked model in Fig. 6b. A similar version of Eq. (6) was originally used by Dyskin et al. (2000) to interpolate intermediate results between two bounding asymptotic values. It has the properties that $K_i = K_i^{beam}$ as $A_0 / h \to \infty$ (i.e., a long crack) and $K_i = K_{i0} + \Delta K_i^{dip}$ as $A_0 / h \to 0$ (i.e., a short crack).

$$K_i = K_{i0} + \frac{\Delta K_i^{dip} + \varepsilon_1 (A_0 / h)^{\varepsilon_2} K_i^{beam}}{1 + \varepsilon_1 (A_0 / h)^{\varepsilon_2}} = K_{i0} + \frac{\varepsilon_3 (A_0 / h)^{\varepsilon_4} + \varepsilon_1 (A_0 / h)^{\varepsilon_2} K_i^{beam}}{1 + \varepsilon_1 (A_0 / h)^{\varepsilon_2}}, \qquad (\varepsilon_2 \geq \varepsilon_4;\ i = I, II) \tag{6}$$

3.2 Crack Propagation Path

Based on the adopted LEFM assumption, a new crack grows once the overall SIF $K_{tot} = \sqrt{K_I^2 + K_{II}^2}$ reaches the fracture toughness K_{IC} of sea ice. Afterwards, the crack propagates along a certain path throughout the whole ice section $O1-O-O4-O3$ and reaches the free boundary.

In terms of the direction of propagation from A_i to A_{i+1}, three criteria are often adopted stating that the crack propagates in the direction θ^* (Moës et al., 1999). These criteria show rather little variation for most engineering applications (Hutchinson and Suo, 1991). In this paper, for the convenience of having an explicit formulation, we adopt the third criteria, with θ^* given by Eq. (7) (Hibbitt et al., 2013).

$$\theta^* = \cos^{-1}\left(\frac{3K_{II}^2 + \sqrt{K_I^4 + 8K_I^2 K_{II}^2}}{K_I^2 + 9K_{II}^2}\right) \tag{7}$$

To predict the crack path, we first numerically evaluate SIFs $K_I(A_i)$ and $K_{II}(A_i)$ given an initial crack geometry A_i; after obtaining the crack's propagation direction θ^* by solving Eq. (7), new crack geometry A_{i+1} can be obtained. The procedure is repeated until the solution-dependent crack path reaches the free boundary, thus yielding the crack path.

3.3 XFEM based Numerical Scheme

Here, we shall adopt a generalised numerical approach to calculate the crack's propagation. To avoid continuous mesh refinement and to capture the stress singularity at the crack tip, an XFEM based numerical scheme (Lu et al., 2017) is utilised. Based on results from the numerical scheme, we aim to provide detailed analytical solutions to the SIFs values for the initial crack in accordance to Eqs. (6) and a study on the crack path trajectories during the crack propagation process.

3.3.1 A brief introduction to XFEM

For a cracked body involving complicated geometries or loading conditions, closed-form analytical solutions in terms of its stress state are usually not available. Thus, numerical methods, e.g., Finite Element Methods (FEM) and its various evolved forms and the Boundary Element Method (BEM), are usually adopted to characterise the stress state near a crack tip (Anderson, 2005). One of the major challenges of various numerical methods are to replicate the 'stress concentration' and 'discontinuities', which involve significant/abrupt changes in field variables (e.g., stress, strain and displacements) near the crack tip and along the crack. Traditionally, rather refined meshes (e.g., a so-called focused mesh) and specially designed elements, e.g., singularity element (Tracey, 1971), were utilised to characterise the field variables near the crack tip. Later, the domain integral approach (Shih et al., 1986, Moran and Shih, 1987) largely increased the calculation efficiency even with a relatively coarse mesh. In this paper, an XFEM based approach is adopted. This approach together with the domain integral method enable us to utilise an even coarser mesh to achieve satisfactory accuracy. The general formulation of the XFEM approach is written in Eq. (8) (see, e.g., (Hibbitt et al., 2013)).

$$\mathbf{u} = \sum_{i=1}^{n} N_i [\mathbf{u}_i + H\mathbf{a}_i + \sum_{m=1}^{4} F_m(r,\theta)\mathbf{b}_i^m] \tag{8}$$

Within Eq. (8), the first term on the RHS represents the conventional FEM with a nodal displacement of $\mathbf{u}_i$ that is multiplied by shape functions N_i. The second term on the RHS applies to the nodes $\mathbf{a}_i$ of the enriched elements that are fully cut through by a crack and describes the displacement jump over the crack by additional multiplication by the Heaviside function H, the ‘jump’ property of which is illustrated in Eq. (9).

$$H(\mathbf{x}) = \begin{cases} 1 & \text{if node } i \text{ with coordinate } \mathbf{x} \text{ is on the RHS of the crack} \\ -1 & \text{otherwise} \end{cases} \tag{9}$$

The third term is applied to the element that encompasses the crack tip, describing the near-tip displacement field by additionally multiplying an asymptotic singularity function $F_m(r,\theta)$, which is expressed in Eq. (10) with polar coordinates r and θ with the origin at the crack tip (see Fig. 9).

$$F_n(r,\theta) = [\sqrt{r}\sin(\theta/2) \quad \sqrt{r}\cos(\theta/2) \quad \sqrt{r}\sin(\theta)\sin(\theta/2) \quad \sqrt{r}\sin(\theta)\cos(\theta/2)] \tag{10}$$

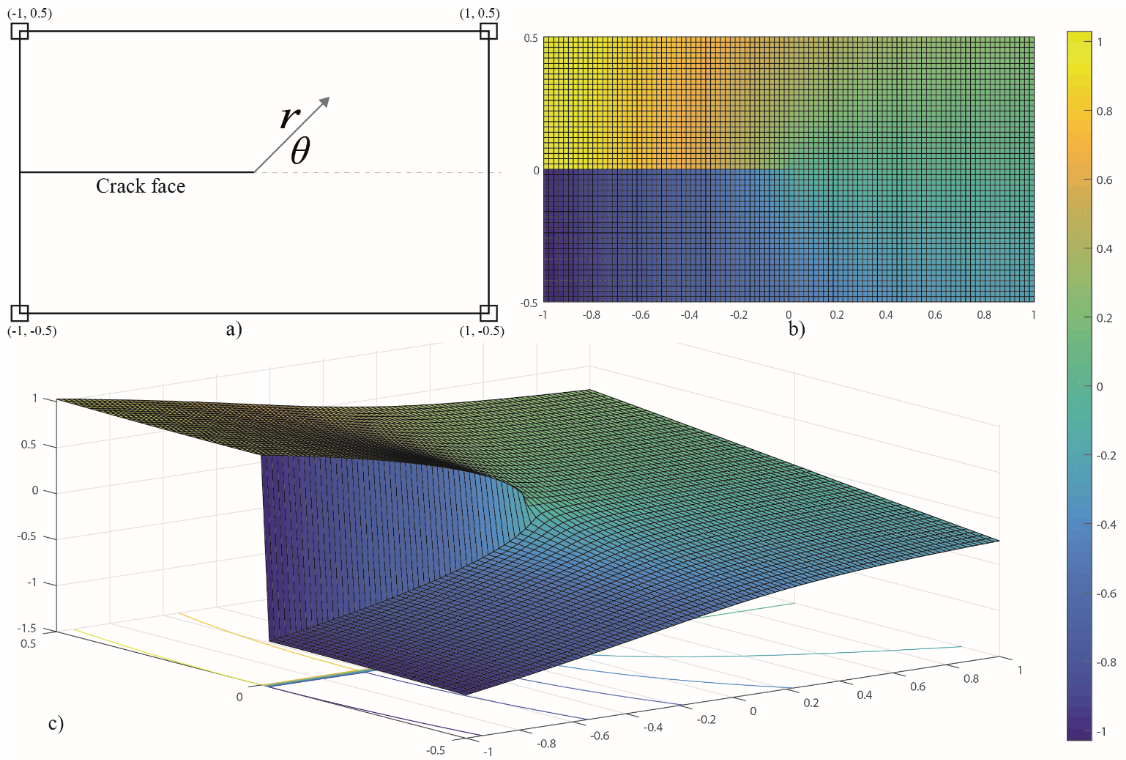

Fig. 9. Enriched element encompassing the crack tip and corresponding leading term of the asymptotic function in Eq. (10).

Notably, the leading term in Eq. (10) introduces a discontinuity along a crack face (i.e., at $\theta = \pm\pi$) within a partially cracked element (Moës et al., 1999, Belytschko and Black, 1999). Following standard FEM procedures, this term is visualised in Fig. 9 with a 2×1 bilinear rectangular element (see Fig. 9a) as an example. This interpolation function is visualised within the partially cracked element in both two- and three- dimensional perspectives in Fig. 9b and c, respectively. The discontinuity at $\theta = \pm\pi$ is illustrated. The asymptotic singularity function $F_m(r, \theta)$ was derived from the closed-form near-crack tip displacement field of a linear elastic and isotropic material under a combination of Mode I and Mode II fractures (e.g., see Eqs. (4, 5) in Belytschko and Black (1999)). The analytical solution to the near-tip behaviour largely increases the simulation efficiency and accuracy. However, if material properties other than linear elastic and isotropic behaviours are encountered, different functions should be adopted. In Eq. (8), both $\mathbf{a}_i$ and $\mathbf{b}_i^m$ are additionally enriched degree of freedoms that are to be calculated given the cracked geometry and loading condition.

3.3.2 A Numerical Scheme for Crack Propagation

In this paper, the XFEM functionality within the ABAQUS/Standard was employed to calculate SIFs K_I and K_{II} via a contour integral method involving the interaction energy release rate formulation (Shih and Asaro, 1988). Afterwards, a numerical scheme is developed to update the crack geometry according to Eq. (7) for each new simulation loop, thereby driving the crack propagation; the scheme has been programmed in MATLAB. The general procedure is illustrated in Fig. 10, and detailed information can be found in (Lu et al., 2017).

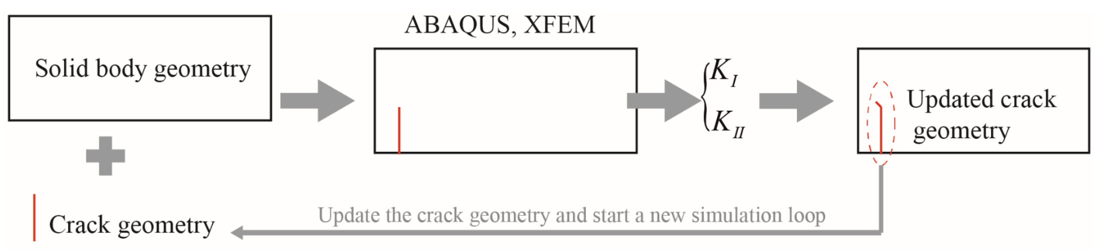

Fig. 10. General procedure of the developed numerical scheme to propagate the crack.

By virtue of XFEM's mesh independency characteristics, the solid body needs to be meshed only once in Fig. 10's numerical scheme. This largely increases the computational efficiency by alleviating us from constantly re-meshing the solid body. In each consecutive simulation, only the crack's geometry is updated according to the calculated SIFs K_I and K_{II} and Eq. (7).

3.3.3 Numerical Set-ups

Based on the previous described numerical method and numerical scheme, the mechanical model in Fig. 6b is solved with the set-ups in Fig. 11. Theoretically, we are expected to calculate models in Fig. 6b with infinite boundaries at *O*2-*O*5 and *O*3-*O*5. However, numerically, it is convenient to define a finite simulation domain. In this regard, we set fixed boundaries *O*2-*O*5 and *O*3-*O*5 far from the crack tip and loading location. Trial simulations were made in-advance to ensure that the boundaries are far enough to be considered as infinitely distant. To cover a large range of A_0/h scenarios and reach asymptotic solutions more effectively, two different geometries are adopted, i.e., geometries catering to the short crack scenario in Fig. 11a and the long crack scenario in Fig. 11b. In these two different geometries, a biased mesh pattern is employed. Fig. 11a and b illustrate the distribution of element nodes in the simulation domain. Dense meshes were utilised near the crack and loading areas such that accurate results can be obtained in the crack propagation simulations. Fig. 11c locally illustrates the mesh pattern together with the loading conditions. Because both the P and Q force components were simulated, a relatively symmetrical mesh pattern towards either side of the crack is adopted.

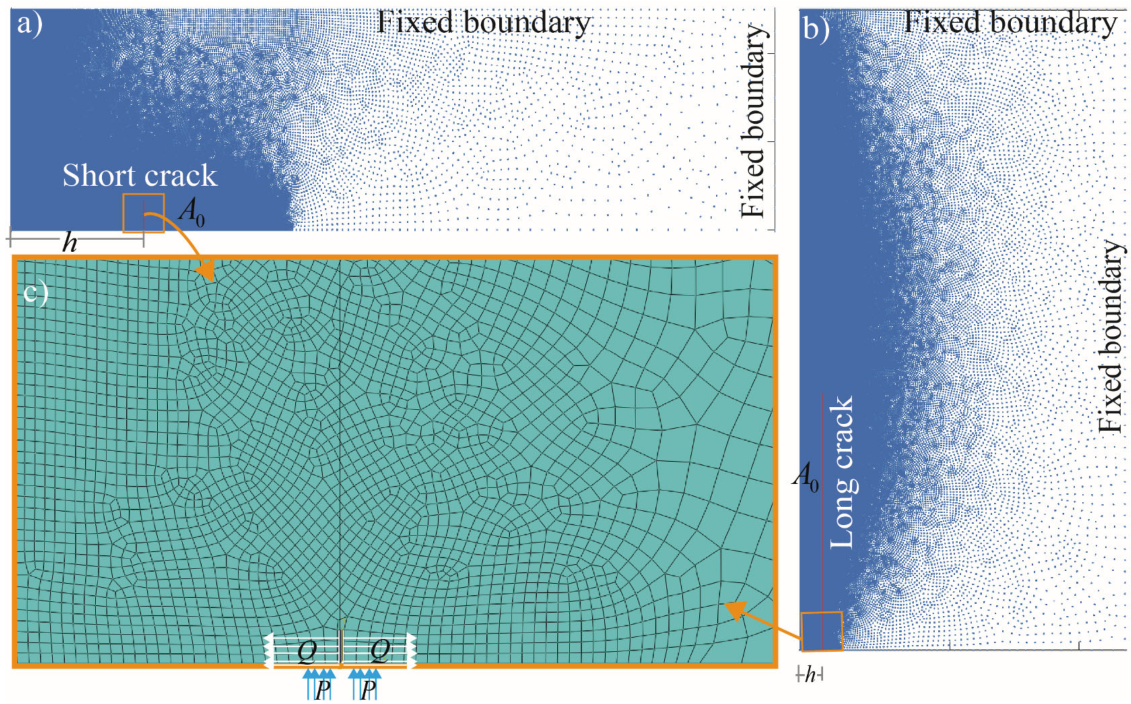

Fig. 11. Numerical set-ups: biased mesh pattern with a) short crack; and b) long crack scenarios; c) mesh pattern near the loading area and initial crack.

Considering the additive nature of linear elastic problems, we simulate two separate loading cases, i.e., Cases #1 ($Q = 1$ and $P = 0$) and #2 ($Q = 0$ and $P = 1$). In the simulations, we varied the ratio of A_0 over h and calculated the corresponding K_I and K_{II}. According to Eq. (6), together with numerical results, parameters $\varepsilon_i (i = 1,2,3,4)$ are fitted to complete Eq. (6). Moreover, following the crack propagation criteria, the crack paths are studied.

4 Benchmark Tests

Before we apply the proposed methods and numerical scheme to our problem, relatively simplified benchmark tests were conducted to validate the numerical model. The benchmark test results are presented herein.

4.1 Calculation of the SIFs

For the edge cracked model in Fig. 6b, analytical solutions exist for the asymptotic scenarios of $A_0 / h \to \infty$ and $A_0 / h \to 0$ (i.e., in Eqs. (3) and (5)). The validity of the adopted numerical model can be proved if the numerical results show similar results towards asymptotic values. Before we use the numerical results for fitting Eq. (6), the asymptotic behaviours of the adopted numerical model in each loading scenario have been satisfactorily benchmarked. More details of this are presented in the results section.

Post-print version of the paper by Lu et al.
in Int J Cold Region of Science and Technology, 156 (2018) 117-133,
https://doi.org/10.1016/j.coldregions.2018.07.010

4.2 Crack path simulation

Next, the proposed numerical scheme's capability for predicting crack paths is studied. In this regard, an off-centre splitting experiment was carried out. The test was conducted on a square shaped ice floe, which was cut free from land-fast sea ice cover at Svea, Svalbard in April 2017. The geometry, initial crack length, and thickness of the ice floe are shown in Fig. 12a. Notably, the initial crack A_0 was prepared 'off-centre'. This is in direct contrast to the test setup described in previous 'fracture properties – oriented tests' (Dempsey et al., 1999a, Dempsey et al., 1999b, Morley and Dempsey, 2015, Lu et al., 2015a), in which a rectangular ice floe was loaded right in the centre. For a centrally loaded test sample, in an ideal condition, the crack is expected to propagate along the centre line due to its symmetry conditions. However, for a test sample loaded off-centre, the crack tends to kink. This is the major motivation behind this test.

The square ice floe shown in Fig. 12a was loaded using a purposely designed jack, which was sufficiently stiff such that little additional compliance was introduced into the entire test system. The jack together with the motor were also sufficiently strong to carry out a displacement-controlled loading scenario. Fig. 12b shows in detail how the splitting force pair F_Y was applied to the prepared ice floe. The initial crack on the ice floe was comprised of two sections. One section (i.e., 140 cm) was cut using a heavy machine (i.e., the DitchWitch described in Lu et al. (2015a)) with a crack width of approximately 10 cm, and the crack tip part (i.e., 10 cm) was cut with a handsaw with a crack width < 3 mm.

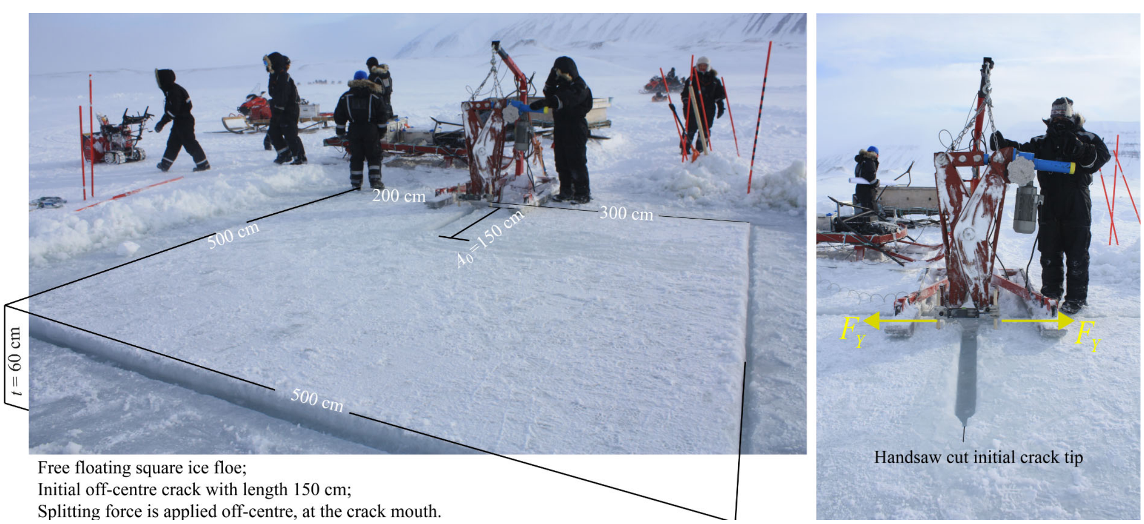

Fig. 12. Field off-centre splitting test set-up.

During the test, the ice floe was free floating with no significant boundary confinement aside from the presence of sea water. The jack's loading speed was 0.6 mm/s, which was considered slow enough such that a quasi-static loading scenario can be assumed. After the test, the crack path was documented by camera images (e.g., see Fig. 13a). With the knowledge of a rectangular shape in the image (i.e., the rectangular frames highlighted by dark lines), a similar image processing technique (see, e.g., (Lu et al., 2016b)) was adopted to rectify Fig. 13a into b without perspective distortion. Thus, the digitalised crack path was obtained, as depicted in Fig. 13b.

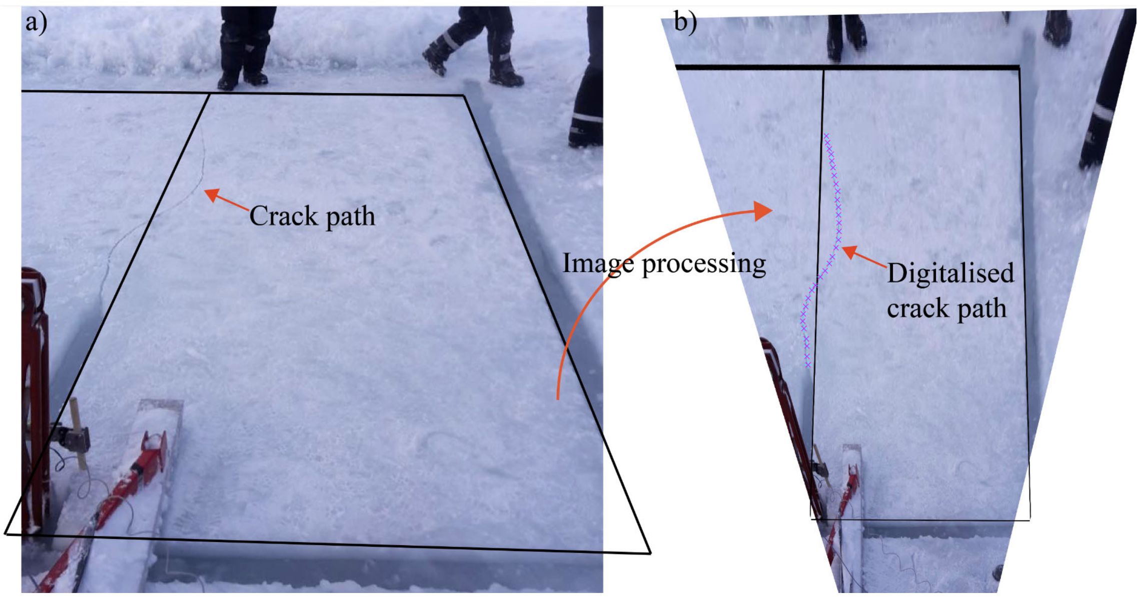

Fig. 13. Crack path after off-centre splitting test.

At the same time, simulations based on the developed scheme in Fig. 10 was conducted. The simulated crack path versus the experiment are illustrated in Fig. 14.

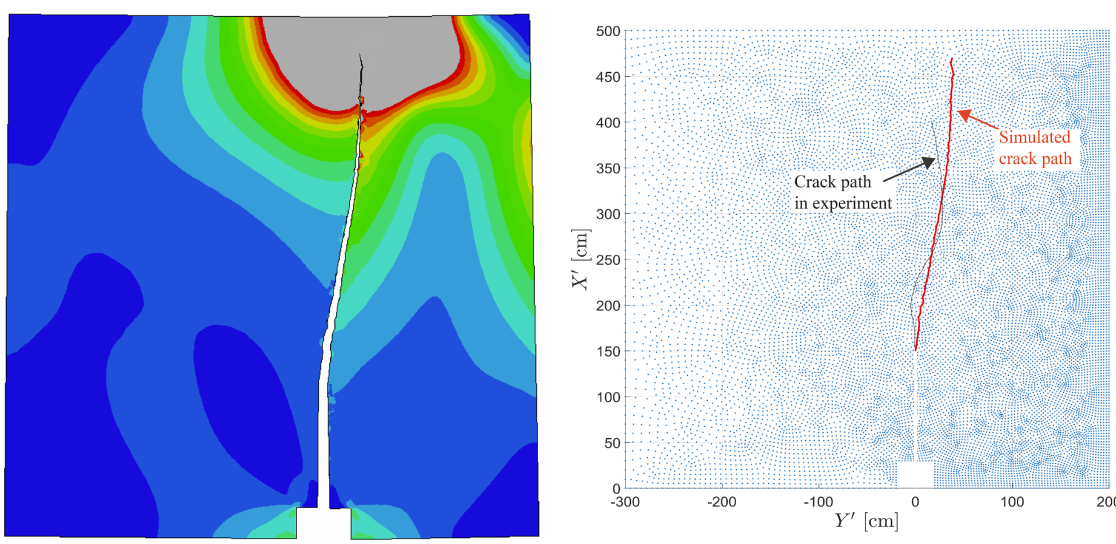

Fig. 14. Crack path of off-centre splitting experiment, a) simulation results; b) a comparison between the experimental and simulated results.

5 Results

After the satisfactory benchmark tests conducted in the previous section, the developed numerical scheme was applied to the proposed test setup in Fig. 11 to study the edge crack's propagation.

5.1 Calculation of Stress Intensity Factors

In terms of the calculations of SIFs, the explicit formulae are developed in the following Eqs. (11) to (16) given the asymptotic constraints in Eqs. (3) and (5). This derivation is based on numerical simulation results with varying A_0 / h values for the numerical setup in Fig. 11. For each loading case, the simulated results, K_I, K_{II} and K_{tot}, are later fitted with the function in Eq. (6), fulfilling the asymptotic constraints. With the obtained fitting parameters, we present the final results in Eqs. (11) to (16).

For loading Case #1 ($Q=1$ and $P=0$), the Mode I and II SIFs are presented in Eqs. (11) and (12).

$$\frac{K_I^Q\sqrt{h}}{Q}=\sqrt{\frac{4\pi}{\pi^2-4}}(\frac{A_0}{h})^{-1/2}+\frac{2.0284(A_0/h)+2.9890}{(A_0/h)^{-1.3569}+1.0499} \tag{11}$$

$$\frac{K_{II}^Q\sqrt{h}}{Q}=\frac{1.8134(A_0/h)+0.5498}{(A_0/h)^{-1.4702}+1.2041} \tag{12}$$

For loading Case #2 ($Q=0$ and $P=1$), the Mode I and II SIFs are presented in Eqs. (13) and (14).

$$\frac{K_I^P\sqrt{h}}{P}=-\frac{2}{\pi}\sqrt{\frac{4\pi}{\pi^2-4}}(\frac{A_0}{h})^{-1/2}+\frac{0.1856\text{-}0.2174(A_0/h)^{0.1635}}{(A_0/h)^{-6.2861}+0.4092(A_0/h)^{0.1635}} \tag{13}$$

$$\frac{K_{II}^P\sqrt{h}}{P}=\frac{0.4051-1.3238(A_0/h)^{0.4339}}{(A_0/h)^{-0.9953}+1.0099(A_0/h)^{0.4339}} \tag{14}$$

Correspondingly, the Mode I and II SIFs under both Q and P are written jointly in Eqs. (15) and (16).

$$\begin{aligned}K_I\sqrt{h}=&\sqrt{\frac{4\pi}{\pi^2-4}}(\frac{A_0}{h})^{-1/2}(Q-\frac{2}{\pi}P)+\\&\frac{2.0284(A_0/h)+2.9890}{(A_0/h)^{-1.3569}+1.0499}Q+\frac{0.1856\text{-}0.2174(A_0/h)^{0.1635}}{(A_0/h)^{-6.2861}+0.4092(A_0/h)^{0.1635}}P\end{aligned} \tag{15}$$

$$K_{II}\sqrt{h}=\frac{1.8134(A_0/h)+0.5498}{(A_0/h)^{-1.4702}+1.2041}Q+\frac{0.4051-1.3238(A_0/h)^{0.4339}}{(A_0/h)^{-0.9953}+1.0099(A_0/h)^{0.4339}}P \tag{16}$$

The fitted Eqs. (11) to (14) are plotted together with the simulation results in Fig. 15. Satisfactory fittings in both the local data points in Fig. 15a and all the data points, i.e., the global behaviour, are illustrated in Fig. 15b. In particular, Fig. 15a demonstrates the $A_0 / h \to 0$ asymptotic behaviour in accordance with Eq. (5) for the P and Q loading condition separately, and Fig. 15b demonstrates the $A_0 / h \to \infty$ behaviour following Eq. (3).

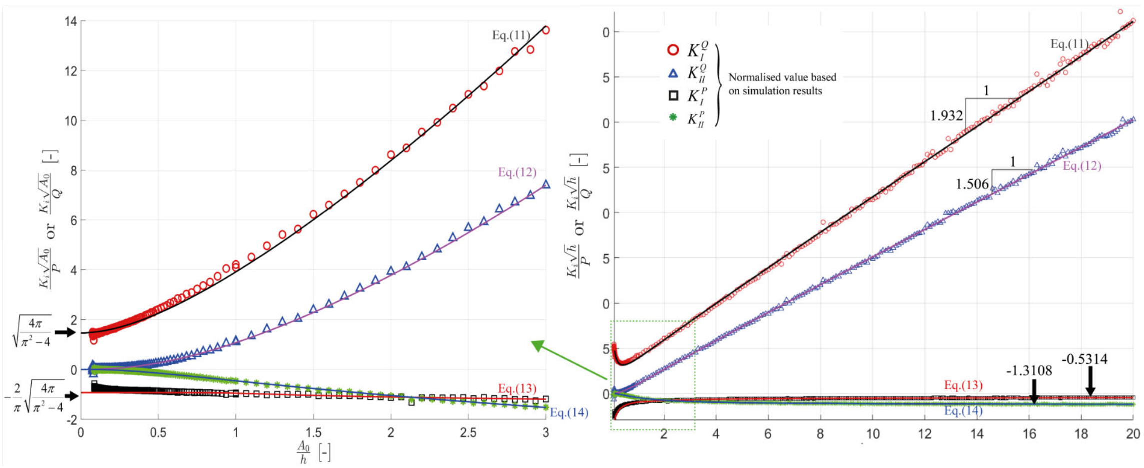

Fig. 15. Simulation results and fitted equations for normalised SIFs, a) local simulated data points with $A_0 / h \to 0$ asymptotic behaviour; b) all simulated data points with $A_0 / h \to \infty$ asymptotic behaviour.

5.2 Crack Propagation Path

Regarding the crack path studies, in this study, our aim is primarily directed to engineering applications. Therefore, precise and thorough crack paths simulations under the complete combinations of P and Q forces and various A_0 / h ratios are not carried out in this paper. Instead, using our developed numerical scheme, we confined our simulations in the region where A_0 / h is approximately 1 and smaller because in the current engineering applications concerning long cracks within two parallel channels, its spacing (i.e., h) is generally larger than the initial crack length A_0. In addition, a careful examination of Eq. (5) shows that a crack ceases to propagate if $Q - 2P / \pi \le 0$ in the limiting scenario of $A_0 / h \to 0$. To achieve generality in the final results and for the current engineering application, we limit our analysis within $P \le 1.5Q$.

First, visual illustrations of the crack paths under different P and Q ratios are presented in Fig. 16 for a particular case with $A_0 / h = 0.6$. Simultaneously, we introduce in Fig. 16a the parameter $L_{\max}$, which can be correlated to the largest size of an ice floe generated between a parallel channel.

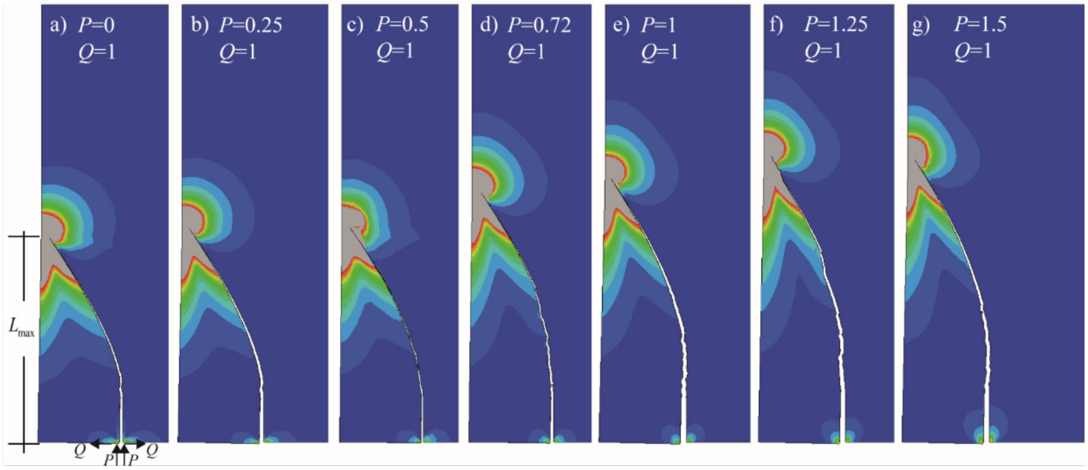

Fig. 16. Visual illustrations of crack paths influenced by various combinations of P and Q for the case $A_0 / h = 0.6$ (Note that only the lower-left part of the simulated domain is illustrated).

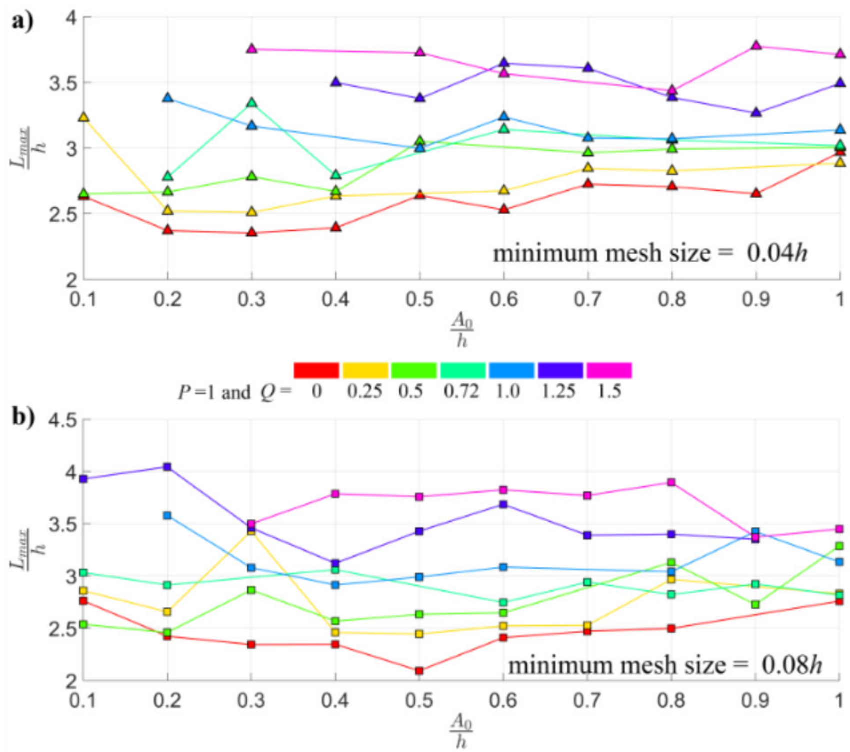

Fig. 17. Summary of XFEM-based numerical simulation results of L_{max} with varying A_0 / h and P / Q ratios.

The complete simulation results concerning L_{max} with varying A_0 / h and P / Q are presented in Fig. 17. For the XFEM based numerical scheme, the utilised mesh sizes shown in the dense mesh region in Fig. 11 were varied for a large number of initial trial simulations until the final simulated crack path became less affected by the chosen mesh size. Fig. 17 presents results for two different mesh sizes, i.e., 0.04 h and 0.08 h .

Post-print version of the paper by Lu et al.
in Int J Cold Region of Science and Technology, 156 (2018) 117-133,
https://doi.org/10.1016/j.coldregions.2018.07.010

In practical applications, it is nontrivial to establish a similar computational mechanics (e.g., XFEM) based numerical scheme to derive $L_{\max}$. Therefore, a relatively simple approach combining the theoretical results in Eqs. (11) to (16) and the numerical results in Fig. 17 is introduced herein to approximate $L_{\max}$. The basic idea is to idealise a kinked crack in Fig. 18a to a scenario in Fig. 18b with a straight crack and an additional moment $M = P\Delta h$ having a tendency to close the crack. Δh is the horizontal (i.e., in Y-direction in Fig. 6) distance between the crack tip and the loading point O. To analytically calculate the SIFs through Eqs. (11) to (16) in this idealised scenario, we further introduce the effective splitting opening force $Q_{eff} = Q - P\Delta h / A$ in an effort to approximate the crack closing effect from the additional moment M. Based on this idealised geometry and loading condition, we assume the actual kink angle in Fig. 18a can be approximated by the model in Fig. 18c with scaling parameters fitted according to numerical results shown in Fig. 17.

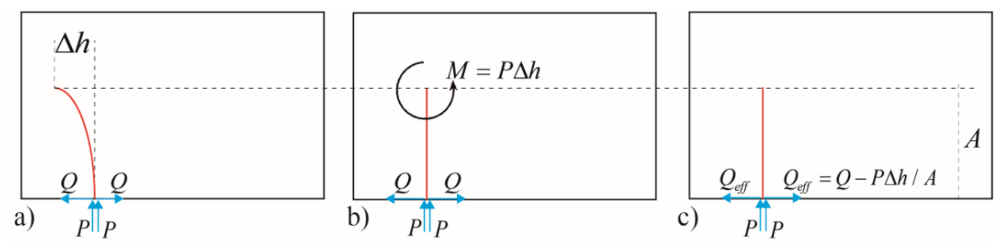

Fig. 18. Idealisation of a kinked crack to straight crack in an off-centre splitting scenario.

Following the above idealisation procedure, the calculation of the intermediate $L'_{\max}$ is achieved via the following numerical recipe.

Table 1. A simple numerical recipe to approximate $L_{\max}$ with derived analytical solutions for SIFs in Fig. 18c.

1. Initialisation of variables for $(i = 1)$, $A_i = A_0$, and $\Delta h = 0$.
2. Introduce the crack advancing step in Y-direction as dh.
3. Starting the numerical loop: **while** $\Delta h < h$, **do**,
   - i. $\Delta h_{i+1} = \Delta h_i + i \cdot dh$.
   - ii. $P = P$, $Q_{eff,i} = Q - P\Delta h_i / A_i$.
   - iii. K_I and K_{II} are calculated according to Eqs. (15) and (16), in which, Q is replaced with the above calculated $Q_{eff,i}$.
   - iv. With known K_I and K_{II}, θ_i^* is calculated according to Eq. (7).
   - v. $\Delta A_i = dh / \tan(\theta_i^*)$, and $A_{i+1} = A_i + \Delta A_i$.
   - vi. $i = i + 1$

At the end of the loop, $L'_{\max} = A_{i+1}$.

Some general calculation results gained from employing the simple numerical recipe in Table 1 are presented in Fig. 19. The numerical recipe grasps these trends: 1) increasing P/Q leads to larger $L'_{\max}$ and 2) increasing A_0/h also leads to larger $L'_{\max}$ but with a relatively milder influence compared to that of P/Q.

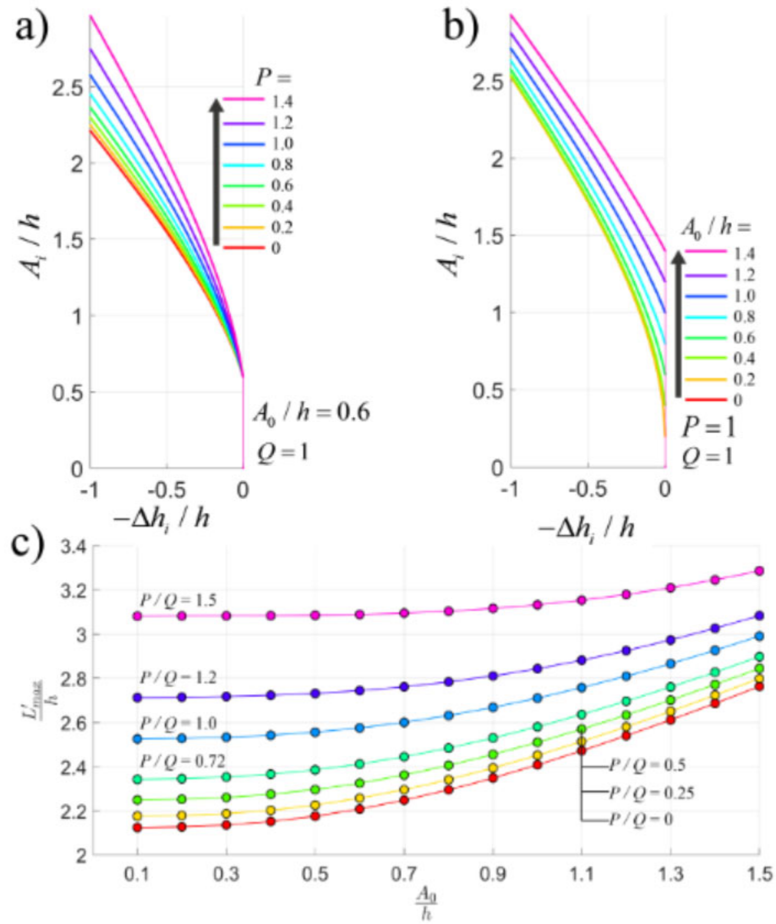

Fig. 19. Crack paths and $L'_{\max}$ calculated using the simple numerical recipe in Table 1, a) crack path with varying P/Q ; b) crack path with varying A_0/h ; and c) $L'_{\max}$ with different combinations of P/Q and A_0/h .

However, the $L'_{\max}$ calculated using Table 1's numerical recipe were generally smaller than the XFEM-based numerical simulation $L_{\max}$ results presented in Fig. 17. Therefore, we scaled $L'_{\max}$ according to Eq. (17) with a linear function of $f_3(P/Q)$, the parameters of which were obtained by a least squares fitting of the numerical results in Fig. 17. The final approximations of $L_{\max}$ with Eq. (17) and Table 1 are presented in Fig. 20.

$$\begin{aligned} L_{\max} &= f_3(P/Q)\cdot L'_{\max} \\ f_3(P/Q) &= 0.0334P/Q+1.1813 \end{aligned} \tag{17}$$

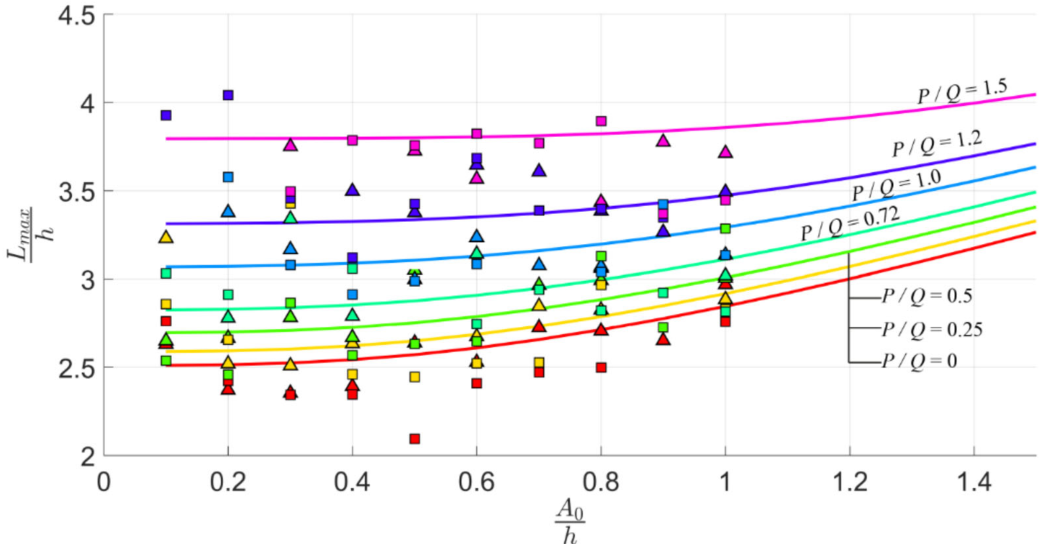

Fig. 20. The calculations of Eq. (17) and Table 1 versus XFEM-based numerical simulation results.

6 Discussion

This paper offers a theoretical explanation of the observed long cracks that frequently develop between two parallel channels during ice management operations. After revisiting the theories concerning ship – level ice interactions and corresponding ice fracture patterns, the theoretical model shown in Fig. 6, i.e., an edge crack scenario, has been proposed to explain the observed parallel channels' fracturing mechanism. The theoretical model was extensively studied using a separately developed numerical scheme based on XFEM. The following discussion is based on the proposed methods and major results.

6.1 XFEM based numerical scheme

The proposed numerical scheme, which is based on XFEM, offers solutions to both Mode I and II SIFs given arbitrary crack geometries and loading conditions. In addition, crack geometry is automatically updated with known SIF information, thereby leading to numerical predictions of crack paths. The capability for calculating SIFs using the numerical scheme is validated in Fig. 15 by showing that the numerical results vary in accordance with the asymptotic trend, which would be expected theoretically. Notably, the simulations were conducted with a relatively coarse mesh but with a much higher efficiency when compared to a series of similar simulations conducted by the authors (Lu et al., 2015c) with a conventional FEM scheme. The increased efficiency enabled us to conduct a considerable amount of simulations within a reasonable period of time, making the predictions of crack paths possible.

Afterwards, a field off-centre splitting experiment was introduced to verify the numerical scheme's capability of predicting the crack paths. The simulated crack paths were solely solution dependent. They depended on the solutions of both K_I and K_{II} and propagated according to Eq. (7). In the benchmark test, an exact match was not achieved, but the general crack propagation direction was captured. This is considered sufficient for the current engineering application, as we are mainly interested in the aspect ratio of ice floes that will be produced between parallel icebreaker channels. Exact crack path predictions are unnecessary if the overall trajectory is captured.

6.2 Analytical formulations on an edge cracked body

The proposed theoretical model, i.e., the edge crack's propagation under different P and Q loading conditions, was studied in this paper. In particular, analytical formulations conforming to the theoretical model's asymptotic behaviours were obtained in Eqs. (11) to (16) based on the fitting numerical simulations presented in Fig. 15. In Eq. (6), the major functional form was initially determined based on asymptotic behaviours following the same method presented by Dyskin et al. (2000); afterwards, only the parameters in the equations were fitted from numerical results with the least squares fitting method. In Fig. 15, one can see that rather satisfactory fittings were achieved between the numerical simulations and proposed formulation. In particular, Fig. 15a and b demonstrate that both the proposed formulations and numerical simulations were asymptotically converging to the theoretical values. This signifies the correctness of both our numerical simulation results and fitted analytical formulations.

Furthermore, as stated before, the edge crack problem is found in a wide range engineering applications. The proposed analytical formulations, i.e., Eqs. (11) to (16), are expected to have a wider outreach than the current engineering application. This is attributed to the fact that Eqs. (11) to (16) are capable of yielding useful SIF calculations over a wide range of A_0 / h values. However, our major engineering application in this paper resides in a range that features relatively small A_0 / h, as depicted in Fig. 6.

Afterwards, the propagation path of the edge crack was studied by a series of simulations with varying P / Q and A_0 / h. The XFEM-based simulation results are presented in Fig. 17, in which the results calculated with two different mesh sizes are presented. Although the simulation results from both mesh sizes were not exactly the same, they both showed a trend whereby the size, $L_{\max}$, increases with increasing A_0 / h or P / Q. This also means that a large contact force $F_X = 2P$ in the surge direction has a tendency to create a long crack that travels farther, thus leading to a large $L_{\max}$. However, P cannot be too much larger than Q, as demonstrated by the limiting scenario in Eq. (5), in which such a splitting crack ceases to open while $P \geq Q\pi / 2 \approx 1.57Q$ or $F_X \geq \pi F_Y$. In such situations, it is expected that the vertical force component F_Z initiates a local bending failure mode to make way for the structure (Lu et al., 2016a).

On the other hand, this XFEM-based numerical scheme is nontrivial to implement in engineering applications to calculate $L_{\max}$. In that regard, we further exploited the analytical formulae in Eqs. (15) and (16) to derive an approximation of $L_{\max}$ based on the idealisation shown in Fig. 18 following the simple numerical recipe presented in Table 1. This simple numerical recipe together with a fitting formula in Eq. (17) yielded relatively reasonable predictions of $L_{\max}$, as demonstrated in Fig. 20. The results of $L_{\max}$ from Table 1 and Eq. (17) combine both information of an idealised crack tip's SIFs under the joint influence of P and Q and XFEM-based numerical simulation results giving rise to a scaling factor $f_3(P/Q)$. The curves in Fig. 20 show similar trends of the XFEM-based numerical simulation in the sense that $L_{\max}$ increases with increasing A_0/h or P/Q, whereas the influence of A_0/h is less pronounced relative to that of P/Q. Most importantly, the numerical recipe in Table 1 is much easier to implement in comparison with the XFEM-based simulation, demonstrating its potential to yield approximations for engineering applications.

These developed analytical formulations (i.e., Eqs. (11) to (17)) and the numerical recipe in Table 1 will be applied to explain the current parallel channels' fracture mechanism. As noted in the beginning, practical engineering questions were sought in this paper, i.e., 1) what is the maximum channel spacing $h_{\max}$ beyond which the long crack ceases to develop and 2) what is the maximum floe size that can be produced between two parallel channels with a given spacing. In the next two sections, these two questions will be discussed by invoking the support of the developed analytical formulations.

6.3 Maximum parallel channel spacing

Eqs. (15) and (16) state the criteria for crack initiation. In other words, in order for any initial crack A_0 in Fig. 6 to further propagate into the observed long cracks, SIFs calculated from Eqs. (15) and (16) should be larger than the fracture toughness of sea ice. After rearranging the equations, we can therefore obtain Eq. (18), in which the maximum channel spacing $h_{\max}$ is given in an implicit form. In Eq. (18), two functions, $f_1(A_0/h, \beta_{YX})$ and $f_2(A_0/h, \beta_{YX})$, are introduced to characterise the influence from A_0/h and P/Q.

The first term in Eq. (18) illustrates $h_{\max}$'s functional dependence with parameters, such as contact force in the surge direction F_X and fracture toughness K_{IC}. Given information of these parameters, one can calculate $h_{\max}$, beyond which, long cracks of Types #1-3 in Fig. 4 cease to occur.

$$
\begin{aligned}
&h_{\max} = (\frac{F_X}{tK_{IC}})^2[f_1^2(\frac{A_0}{h_{\max}},\beta_{YX}) + f_2^2(\frac{A_0}{h_{\max}},\beta_{YX})] \\
&\beta_{YX} = \frac{F_Y}{F_X} = \frac{Q}{2P} \\
&f_1(\frac{A_0}{h},\beta_{YX}) = \sqrt{\frac{4\pi}{\pi^2-4}}(\frac{A_0}{h})^{-1/2}(\beta_{YX}-\frac{1}{\pi}) + \frac{2.0284(A_0/h)+2.9890}{(A_0/h)^{-1.3569}+1.0499}\beta_{YX} + \frac{1}{2}\frac{0.1856\text{-}0.2174(A_0/h)^{0.1635}}{(A_0/h)^{-6.2861}+0.4092(A_0/h)^{0.1635}} \\
&f_2(\frac{A_0}{h},\beta_{YX}) = \frac{1.8134(A_0/h)+0.5498}{(A_0/h)^{-1.4702}+1.2041}\beta_{YX} + \frac{1}{2}\frac{0.4051-1.3238(A_0/h)^{0.4339}}{(A_0/h)^{-0.9953}+1.0099(A_0/h)^{0.4339}}
\end{aligned}
\tag{18}
$$

In Eq. (18), there is another undetermined parameter, i.e., the initial crack length A_0. This initial crack length is considered to be introduced by the radial cracking process at the ship stem (see Fig. 3). According to previous studies (Lu et al., 2015c, Sodhi, 1996), the maximum length the radial crack length can reach is $A_0 = 2\ell$, in which ℓ is the characteristic length for an elastic plate on a Winkler type foundation. Its expression is written in Eq. (19):

$$\ell = \sqrt[4]{D/k}\ , \tag{19}$$

in which

$D = Et^3/[12(1-\nu^2)]$	is the flexural rigidity of an elastic plate expressed with material properties of Young's modulus E and Poisson ratio ν; and
$k = \rho_w g$	is the foundation stiffness. In this case, it is expressed by the sea water density ρ_w and gravitational acceleration g.

In the sequel paper (Paper II), a series of well-controlled field experiments are reported, and comparisons are presented. It is reminded here that by utilising Eq. (18), an upper limit $h_{\max}$ is solved, i.e., parallel channel spacings exceeding $h_{\max}$ will lead to the absence of long cracks, as in Fig. 5. On the other hand, a channel spacing $h < h_{\max}$ does not necessitate the occurrence of long cracks due to other important factors that are not studied in this paper, e.g., initial crack formation, location and orientation and the required crack propagation force history, which might become sufficiently large to prohibit further development of a long crack although it has been initiated according to (18).

6.4 Floe size ratio production

Suppose that the channel spacing $h < h_{\max}$ and a long crack of Type #1 in Fig. 4 is formed. Based on the study of crack paths and definition of $L_{\max}$ (see Fig. 16), we can first define, in a conventional way, the floe size as the Mean Calliper Diameter (MCD) L_{MCD} as Eq. (20),

$$L_{MCD} = \sqrt{4(L_{\max} h)/\pi} \quad , \tag{20}$$

or in floe ratio form shown in Eq. (21).

$$\text{floe ratio} = L_{MCD} / h = \sqrt{4(L_{\max} / h)/\pi} \tag{21}$$

Given the formulations on $L_{\max}$ based on Eq. (17) and Table 1, Eq. (21) is plotted in Fig. 21 to illustrate the relationship between generated floe size L_{MCD} versus channel spacing h for ice thicknesses $t = 1$ m and 2 m. In the figure, reference curves with $L_{MCD} = 2h$ and $L_{MCD} = h$ are also illustrated.

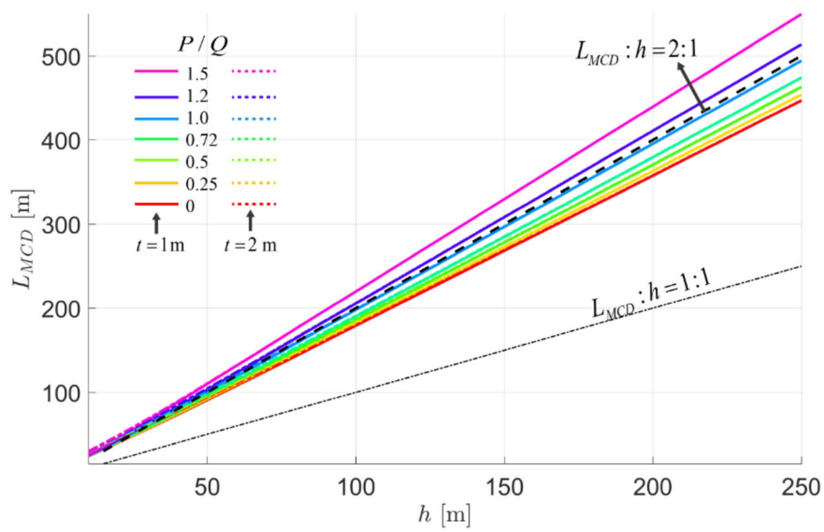

Fig. 21. The maximum possible ice floe size L_{MCD} versus channel spacing h .

Fig. 21 shows that most of the floe sizes L_{MCD} are rather close to the approximation of $L_{MCD} \approx 2h$, although a larger ratio of P/Q leads to larger L_{MCD} . Fig. 21 also shows that there is no significant influence on L_{MCD} from ice thickness. Ice thickness is important in determining whether such a long crack occurs, but once such long cracks are formed, the eventual floe size is less dependent on ice thickness.

In particular, the curve $L_{MCD} = h$ shown in Fig. 21 has often been used to characterise the floe size between two parallel channels (e.g., in (Hamilton et al., 2011b)). Fig. 21 shows that L_{MCD} can exceed h. However, it is important to stress the physical meaning of L_{MCD}, which is the maximum possible ice floe size that is produced according to the discussed parallel channel fracturing mechanism. It does not characterise how frequently such maximum ice floes are produced. In reality, fractures of different types, e.g., Types #1-4 in Fig. 5, occur. This creates ice floes with various sizes, shapes and aspect ratios. In the sequel Paper II, field experiments are conducted to quantify all the floe sizes within parallel channels, and it can be shown that for the majority (i.e., to the extent of 80%) of ice floes, the sizes $L_{MCD} \le h$. For now, the formulation of L_{MCD} is of theoretical importance in the sense of drawing a border in terms of the maximum possible floe size that can be produced. Later, study shall explore its corresponding floe size distribution.

6.5 Limitations of the theoretical model

The studied theoretical model in Fig. 6 has limitations to explain the complete parallel channels' fracturing mechanism. After all, we focus mainly on the in-plane splitting type failures and the influence of out-of-plane contact force F_Z is not included in the preceding analysis. Moreover, among all the possible in-plane crack patterns (see Fig. 4), we focus on the scenario with Crack #1. In the field, ice floes of various sizes were generated in between two parallel channels by the joint effects of both in-plane and out-of-plane contact forces and also various splitting scenarios in Fig. 4. The proposed theoretical model in Fig. 6 primarily focus on an upper threshold scenario in terms of the largest ice floe L_{MCD} and maximum channel spacing $h_{\max}$. The statistical floe size distribution within parallel channels shall be studied in the sequel Paper II.

7 Conclusions

Based on a review and discussion of the theories regarding level ice – ship interactions, the physics behind parallel channel fracture mechanisms were presented. The observed long cracks between two parallel channels are considered to be caused by the presence of a nearby free boundary. In lieu of this, a theoretical model involving the splitting of an edge crack has been proposed in this paper. The model was extensively studied using a separately and purposely developed eXtended Finite Element Method (XFEM) based numerical scheme. Before the actual studies were undertaken on the target theoretical model, benchmark tests were conducted, and satisfactory confidence were gained on the validity of the proposed numerical scheme.

With the XFEM based numerical scheme, two issues were investigated regarding the proposed theoretical model: the propagation of a pre-existing radial crack and its sequential crack path. Based on extensive numerical simulations and theoretical analysis, two groups of important formulations were proposed. These two groups of equations are in direct response to the practical questions raised in this paper.

The first group of equations (i.e., Eqs. (11) to (16)) were obtained by first constructing a formula form following the stated problem's asymptotic analysis, and the formula's parameters were then fitted from the XFEM-based numerical calculation results. These equations enable us to calculate the Stress Intensity Factors (SIFs) of an edge cracked body with a wide range of ratios between initial crack length A_0 and the edge crack's width h and the ratio between the crack parallel force P and the crack orthogonal force Q. Practically, this group of equations is converted into Eq. (18), which allows us to determine if a long crack between two parallel channels would occur at all. In another words, if the parallel channel's spacing exceeds a threshold $h_{\max}$ (expressed in Eq. (18)), the potential parallel channel fracture mechanism is not expected.

The second group of equations and algorithm (i.e., Eq. (17) and a numerical recipe in Table 1) characterise the crack path of an edge crack. The closed-form and simplified crack paths were obtained from an idealised cracked geometry analysis using the previously derived Eqs. (11) to (16), yielding an initial approximation of $L_{\max}$ (defined in Fig. 16, giving a certain measure of generated floe size). The actual $L_{\max}$ is scaled up in Eq. (17) via fitting numerical results from the XFEM-based simulation of crack paths. Practically, the studied crack path represents the observed long cracks' profiles between two parallel channels, the knowledge of which sheds light on the produced ice floes' size ratios and their possible maximum size L_{MCD}. Further formulations of floe size ratio or L_{MCD} were given in Eqs. (20) and (21).

The obtained equations are the major contributions of this paper. In particular, Eqs. (11) to (16) are expected to have a wider outreach in terms of edge crack problems. Given the above equations, practical applications were thoroughly demonstrated and discussed. In the associated Paper II, these equations shall be further verified by a group of well-controlled field experiments concerning parallel channels' fracturing mechanism. In that paper, more quantifiable results will be provided.

Acknowledgements

The Oden Arctic Technology Research Cruise 2015 (OATRC2015) was supported by the ExxonMobil Upstream Research Company and performed by the Norwegian University of Science and Technology (NTNU) in cooperation with the Swedish Polar Research Secretariat (SPRS) and the Swedish Maritime Administration (SMA). In addition, OATRC2013, which was sponsored by Statoil, is also acknowledged because part of the data was used for this paper.

References

ANDERSON, T. L. 2005. *Fracture mechanics: fundamentals and applications*, CRC press.

BAŽANT, Z. P. 2002a. Scaling of sea ice fracture-Part I: Vertical penetration. *Journal of applied mechanics,* 69**,** 11-18.

BAŽANT, Z. P. 2002b. Scaling of sea ice fracture-Part II: Horizontal load from moving ice. *Journal of applied mechanics,* 69**,** 19-24.

BAŽANT, Z. P. & PLANAS, J. 1998. *Fracture and size effect in concrete and other quasibrittle materials*, CRC.

BELYTSCHKO, T. & BLACK, T. 1999. Elastic crack growth in finite elements with minimal remeshing. *International Journal for Numerical Methods in Engineering,* 45**,** 601-620.

BHAT, S. U. 1988. Analysis for splitting of ice floes during summer impact. *Cold Regions Science and Technology,* 15**,** 53-63.

BHAT, S. U., CHOI, S. K., WIERZBICKI, T. & KARR, D. G. 1991. Failure analysis of impacting ice floes. *Journal of Offshore Mechanics and Arctic Engineering,* 113**,** 171.

BJØRKLUND, H., SINITSYN, A. & PRUSAKOV, A. 2015. 360 Camera System for Mornitoring Ice Conditions. *Proceedings of the 23rd International Conference on Port and Ocean Engineering under Arctic Conditions.* Trondheim, Norway.

DEMPSEY, J. P. 1991. The fracture toughness of ice. *Ice-Structure Interaction***,** 109–145.

DEMPSEY, J. P., ADAMSON, R. M. & MULMULE, S. V. 1999a. Scale effects on the in-situ tensile strength and fracture of ice. Part II: First-year sea ice at Resolute, NWT. *International journal of fracture,* 95**,** 347-366.

DEMPSEY, J. P., DEFRANCO, S. J., ADAMSON, R. M. & MULMULE, S. V. 1999b. Scale effects on the in-situ tensile strength and fracture of ice Part I: Large grained freshwater ice at Spray Lakes Reservoir, Alberta. *International journal of fracture,* 95**,** 325-345.

DEMPSEY, J. P., DEFRANCO, S. J., BLANCHET, D. & PRODANOVIC, A. Splitting of ice floes. 1st International Conference: Development of Russian Arctic Offshore (RAO'93), 1993.

DEMPSEY, J. P. & MU, Z. 2014. Weight function for an edge-cracked rectangular plate. *Engineering Fracture Mechanics,* 132**,** 93-103.

DYSKIN, A. V., GERMANOVICH, L. N. & USTINOV, K. B. 2000. Asymptotic analysis of crack interaction with free boundary. *International Journal of Solids and Structures,* 37**,** 857-886.

ENKVIST, E., VARSTA, P. & RISKA, K. The ship-ice interaction. Proceedings of the 5th International Conference on Port and Ocean Engineering under Arctic Conditions., 1979 Norwegian Institute og Technology, Trondheim, Norway. 977-1002.

ETTEMA, R., STERN, F. & LAZARO, J. 1989. Dynamics of continuous-mode icebreaking by a polar-class icebreaker hull. *Journal of Ship Research,* 33**,** 115-134.

EVANS, A., PALMER, A., GOODMAN, D., ASHBY, M., HUTCHINSON, J., PONTER, A. & WILLIAMS, G. Indentation spalling of edge-loaded ice sheets. Proceedings of ICE: the 7th International Symposium (on Ice) of the International Association for Hydraulic Research, 1984. IAHR, 113-121.

FARID, F., SCIBILIA, F., LUBBAD, R. & LØSET, S. 2014. Sea Ice Management Trials during Oden Arctic Technology Research Cruise 2013 Offshore North East Greenland. *22nd IAHR International Symposium on Ice.* Singapore.

FREUND, L. B. 1978. Stress intensity factor calculations based on a conservation integral. *International Journal of Solids and Structures,* 14**,** 241-250.

HAMILTON, J., HOLUB, C., BLUNT, J., MITCHELL, D. & KOKKINIS, T. Ice Management for Support of Arctic Floating Operations. OTC Arctic Technology Conference, 2011a.

HAMILTON, J., HOLUB, C. J. & BLUNT, J. 2011b. Simulation of ice management fleet operations using two decades of Beaufort Sea ice drift and thickness time histories. *Proceedings of International Society of Offshore and Polar Engineers (ISOPE), Maui, Hawaii.*

HAMILTON, J., KOKKINIS, T., HOLUB, C., MATSKEVITCH, D., CHENG, T., HARRIS, M. & SHAFROVA, S. Near-Field Ice Management Tactics for Floating Drilling in Arctic Pack Ice. Arctic Technology Conference, 2016. Offshore Technology Conference.

HIBBITT, KARLSSON & SORENSEN 2013. *ABAQUS/Standard user's manual*, Hibbitt, Karlsson & Sorensen.

HILLERBORG, A., MODEER, M. & PETERSSON, P. E. 1976. Analysis of crack formation and crack growth in concrete by means of fracture mechanics and finite elements. *Cement and concrete research,* 6**,** 773-781.

HUTCHINSON, J. W. & SUO, Z. 1991. Mixed mode cracking in layered materials. *Advances in applied mechanics,* 29**,** 63-191.

KASHTELJAN, V. I., POZNJAK, I. I., RYVLIN, A. J. & CORPORATION, M. C. A. 1969. *Ice Resistance to Motion of a Ship*, Marine Computer Application Corporation.

KERR, A. D. 1976. The bearing capacity of floating ice plates subjected to static or quasi-static loads. *Journal of Glaciology,* 17**,** 229-268.

KOTRAS, T. V., BAIRD, A. V. & NAEGLE, J. N. Predicting Ship Performance in Level Ice. 1983 New York, NY, USA. SNAME, 329-349.

LEWIS, J. W. & EDWARDS, J. R. Y. 1969. Predicting Icebreaking Capabilities of Icebreakers.

LINDQVIST, G. A straightforward method for calculation of ice resistance of ships. Proceedings of POAC 1989, 1989. 722-735.

LU, W. 2014. *Floe Ice - Sloping Structure Interactions.* Doctor of Philosophy Doctoral, Norwegian University of Science and Technology.

LU, W., HEYN, H.-M., LUBBAD, R. & LØSET, S. 2017. Large Scale Simulations of Floe-ice Fractures and Validation against Full-scale Data. *International Conference on Port and Ocean Engineering under Arctic Conditions* Busan, Korea.

LU, W., LØSET, S., SHESTOVE, A. & LUBBAD, R. Design of a field test for measuring the fracture toughness of sea ice. *In:* KIM, E., LU, W. & HØYLAND, K., eds. The 23rd International Conference on Port and Ocean Engineering under Arctic Conditions, June 14-18, 2015 2015a Trondheim, Norway.

LU, W., LUBBAD, R. & LØSET, S. 2015b. In-plane fracture of an ice floe: A theoretical study on the splitting failure mode. *Cold Regions Science and Technology,* 110**,** 77-101.

LU, W., LUBBAD, R. & LØSET, S. 2015c. Out-of-plane failure of an ice floe: Radial-crack-initiation-controlled fracture. *Cold Regions Science and Technology,* 119**,** 183-203.

LU, W., LUBBAD, R. & LØSET, S. Tentative Fracture Mechanisms of the Parallel Channel Effect During Ice Management. *In:* KIM, E., LU, W. & HØYLAND, K., eds. The 23rd International Conference on Port and Ocean Engineering under Arctic Conditions, 14-18 June 2015, 2015d Trondheim, Norway.

LU, W., LUBBAD, R., LØSET, S. & KASHAFUTDINOV, M. 2016a. Fracture of an ice floe: Local out-of-plane flexural failures versus global in-plane splitting failure. *Cold Regions Science and Technology,* 123**,** 1-13.

LU, W., ZHANG, Q., LUBBAD, R., LØSET, S. & SKJETNE, R. 2016b. A Shipborne Measurement System to Acquire Sea Ice Thickness and Concentration at Engineering Scale. *Arctic Technology Conference 2016.* St. John's, Newfoundland and Labrador.

LUBBAD, R. & LØSET, S. 2011. A numerical model for real-time simulation of ship-ice interaction. *Cold Regions Science and Technology,* 65**,** 111-127.

LUBBAD, R. & LØSET, S. Time Domain Analysis of Floe Ice Interactions with Floating Structures. OTC Arctic Technology Conference, 2015. Offshore Technology Conference.

LUBBAD, R., LØSET, S., HEDMAN, U., HOLUB, C. & MATSKEVITCH, D. 2016. Oden Arctic Technology Research Cruise 2015. *Proc. of the Arctic Technology Conference (ATC).* St. Johns's, Newfoundland and Labardor, Canada.

LUBBAD, R., LØSET, S., LU, W., TSARAU, A. & VAN DEN BERG, M. 2018. An overview of the Oden Arctic Technology Research Cruise 2015 (OATRC2015) and numerical simulations performed with SAMS driven by data collected during the cruise. *Cold Regions Science and Technology*.

MILANO, V. R. 1972. *Ship resistance to continuous motion in ice.* Stevens Institute of Technology.

MOËS, N., DOLBOW, J. & BELYTSCHKO, T. 1999. A finite element method for crack growth without remeshing. *Int. J. Numer. Meth. Engng,* 46**,** 131-150.

MORAN, B. & SHIH, C. F. 1987. A general treatment of crack tip contour integrals. *International Journal of Fracture,* 35**,** 295-310.

MORLEY, G. & DEMPSEY, J. P. A Workman's Guide to In Situ Sea Ice Fracture Testing. Proceedings of the 23rd International Conference on Port and Ocean Engineering under Arctic Conditions, 2015 Trondheim, Norway.

MULMULE, S. V. & DEMPSEY, J. P. 1998. A viscoelastic fictitious crack model for the fracture of sea ice. *Mechanics of Time-dependent Materials,* 1**,** 331-356.

MULMULE, S. V. & DEMPSEY, J. P. 2000. LEFM size requirements for the fracture testing of sea ice. *International journal of fracture,* 102**,** 85-98.

NAEGLE, J. N. 1980. *Ice-Resistance Prediction and Motion Simulation For Ships Operating in The Continuous Mode of Icebreaking.* The University of Michigan.

RENSHAW, C. E. & SCHULSON, E. M. 2001. Universal behaviour in compressive failure of brittle materials. *Nature,* 412**,** 897-900.

RISKA, K. 2011. Ship–Ice Interactions In Ship Design: Theory and Practice. *Course Material NTNU.* Trondheim.

SAWAMURA, J., RISKA, K. & MOAN, T. 2009. Numerical Simulation of Breaking Patterns in Level Ice at Ship's Bow. *Proceedings of the Nineteenth (2009) International Offshore and Polar Engineering Conference.* Osaka, Japan.

SCHULSON, E. M. & DUVAL, P. 2009. *Creep and fracture of ice,* Cambridge, Cambridge University Press.

SHIH, C. & ASARO, R. 1988. Elastic-plastic analysis of cracks on bimaterial interfaces: part I—small scale yielding. *Journal of Applied Mechanics,* 55**,** 299-316.

SHIH, C. F., MORAN, B. & NAKAMURA, T. 1986. Energy release rate along a three-dimensional crack front in a thermally stressed body. *International Journal of Fracture,* 30**,** 79-102.

SODHI, D. S. Deflection Analysis of Radially Cracked Floating Ice Sheets. OMAE, 1996. 97-102.

SU, B., RISKA, K. & MOAN, T. 2010. A numerical method for the prediction of ship performance in level ice. *Cold Regions Science and Technology,* 60**,** 177-188.

TADA, H., PARIS, P. C. & IRWIN, G. R. 2000. *The stress analysis of cracks handbook*, ASME press New York.

TAN, X., SU, B., RISKA, K. & MOAN, T. 2013. A six-degrees-of-freedom numerical model for level ice–ship interaction. *Cold Regions Science and Technology,* 92**,** 1-16.

THOULESS, M. D. & EVANS, A. G. 1990. Comment on the spalling and edge-cracking of plates. *Scripta Metallurgica et Materialia,* 24**,** 1507-1510.

THOULESS, M. D., EVANS, A. G., ASHBY, M. F. & HUTCHINSON, J. W. 1987. The edge cracking and spalling of brittle plates. *Acta Metallurgica,* 35**,** 1333-1341.

TRACEY, D. M. 1971. Finite elements for determination of crack tip elastic stress intensity factors. *Engineering Fracture Mechanics,* 3**,** 255-265.

VALANTO, P. On the cause and distribution of resistance forces on ship hulls moving in level ice. Proceedings of the 18th International Conference on Port and Ocean Engineering under Arctic Conditions, August 12-17, 2001 2001 Ottawa, Ontario, Canada. 803-816.

ZLATIN, A. & KHRAPKOV, A. A semi-infinite crack parallel to the boundary of the elastic half-plane. Soviet Physics Doklady, 1986. 1009.

ZLATIN, A. & KHRAPKOV, A. 1990. Elastic Half-Plane Weakened by a Crack Parallel to Its Boundary. *Studies in Elasticity and Plasticity,* 16**,** 68-75.